Precambrian Research 183 (2010) 635–659

Contents lists available at ScienceDirect

Precambrian Research

journal homepage: www.elsevier.com/locate/precamres

Paleoproterozoic gabbronoritic and granitic magmatism in the northern margin of the North China craton: Evidence of crust–mantle interaction

Peng Peng[a,b,*], Jinghui Guo[a], Mingguo Zhai[a], Wouter Bleeker[b]

[a] State Key Laboratory of Lithospheric Evolution, Institute of Geology and Geophysics, Chinese Academy of Sciences, Beijing 100029, China
[b] Geological Survey of Canada, Ottawa K1A 0E9, Canada

ARTICLE INFO

Article history:
Received 30 April 2009
Received in revised form 5 August 2010
Accepted 19 August 2010

Keywords:
North China craton
Paleoproterozoic
Gabbronorite
Dyke and sill
Ultra-high-temperature metamorphism
Crust–mantle interaction
Ridge subduction

ABSTRACT

Paleoproterozoic Xuwujia gabbronorites in the northern margin of the North China craton occur as dykes, sills and small plutons intruded into khondalite (aluminous paragneisses, sedimentary protoliths deposited at ca. 2.0–1.95 Ga), and as numerous entrained bodies and fragments of variable scales in the Liangcheng granitoids (ca. 1.93–1.89 Ga). These gabbronoritic dykes are present at all locations where ca. 1.93–1.92 Ga ultra-high-temperature metamorphism is recorded in the khondalite. A gabbronorite sample from the Hongmiaozi dyke gives zircon $^{207}Pb/^{206}Pb$ mean ages of 1954 ± 6 Ma (core domains) and 1925 ± 8 Ma (rim domains). These ages, as well as previously reported ages, constrain the age of mafic magmatism to be at ca. 1.96–1.92 Ga (~1.93 Ga). One sample from the Xigou gabbro intruded by the Liangcheng granitoids gives a zircon $^{207}Pb/^{206}Pb$ mean age of 1857 ± 4 Ma, which is interpreted as the age of a metamorphic overprint. The Xuwujia gabbronorites comprise mainly gabbronorite compositions, as well as some norite, olivine gabbronorite, monzonorite, quartz gabbronorite, and quartz monzonorite. Chemically, they are tholeiitic and can be divided into two groups: a high-Mg group (6.2–22.9 wt.% MgO) and a relatively low-Mg group (2.2–5.7 wt.% MgO). The high-Mg group shows negative Eu-anomalies (Eu/Eu* = 0.53–0.72), slight light rare earth element enrichment (La/Yb_N = 0.56–1.53), and small negative anomalies in high field-strength elements. The εNd (t = 1.93 Ga) values vary from +0.3 to +2.4. The low-Mg group shows varied Eu-anomalies (Eu/Eu* = 0.48–1.05), and is enriched in light rare earth elements (La/Yb_N = 1.51–11.98). The majority shows negative anomalies in high field-strength elements (e.g., Th, Nb, Zr, and Ti). Initial εNd (at 1.93 Ga) values for low-Mg gabbronorites vary from −5.0 to 0. The Xuwujia gabbronorites possibly experienced assimilation of crust, and fractional crystallization of initially olivine and hypersthene (the high-Mg group), and then olivine, clinopyroxene, and plagioclase (the low-Mg group). The slightly younger Liangcheng granitoids consist of garnet-bearing granite, granodiorite and quartz-rich granitic compositions. They are intermediate to felsic calc-alkaline rocks, thought to be derived from surrounding metasedimentary crust. Xigou gabbro could represent early cumulates. The granitoids have relatively high-Mg numbers (up to 54), and show some chemical affinities with the gabbronorites, which could have resulted from incorporation of gabbronoritic melts. The occurrence and chemical variations of the Xuwujia gabbronorites and Liangcheng granitoids can be interpreted to have resulted from crust–mantle interaction, with mingling and partial mixing of mantle (gabbronoritic) and crustal (granitic) melts. The Xuwujia gabbronorites originated from a mantle region with high potential temperatures (~1550 °C), possibly associated with a plume or more likely a ridge-subduction-related mantle upwelling event. They could have had extremely high primary intrusion temperatures (up to 1400 °C). Emplacement of these magmas was likely responsible for the extensive crustal anatexis (Liangcheng granitoids) and the local ultra-high-temperature metamorphism. These sequences may have followed ca. 1.95 Ga continent–continent (arc?) juxtaposition and were themselves followed by significant regional uplift and exhumation in the northern margin of the North China craton.

1. Introduction

Mantle-derived melts ascend and contribute to growth of the continental crust, a process that may also involve subsequent differentiation and/or re-melting (e.g., Anderson, 1987; Taylor and McLennan, 1995; Rudnick and Fountain, 1995). Furthermore, such

* Corresponding author at: State Key Laboratory of Lithospheric Evolution, Institute of Geology and Geophysics, Chinese Academy of Sciences, Beijing 100029, China.
E-mail addresses: pengpengwj@mail.iggcas.ac.cn, pengpengwj@hotmail.com (P. Peng).

0301-9268/$ – see front matter © 2010 Elsevier B.V. All rights reserved.
doi:10.1016/j.precamres.2010.08.015

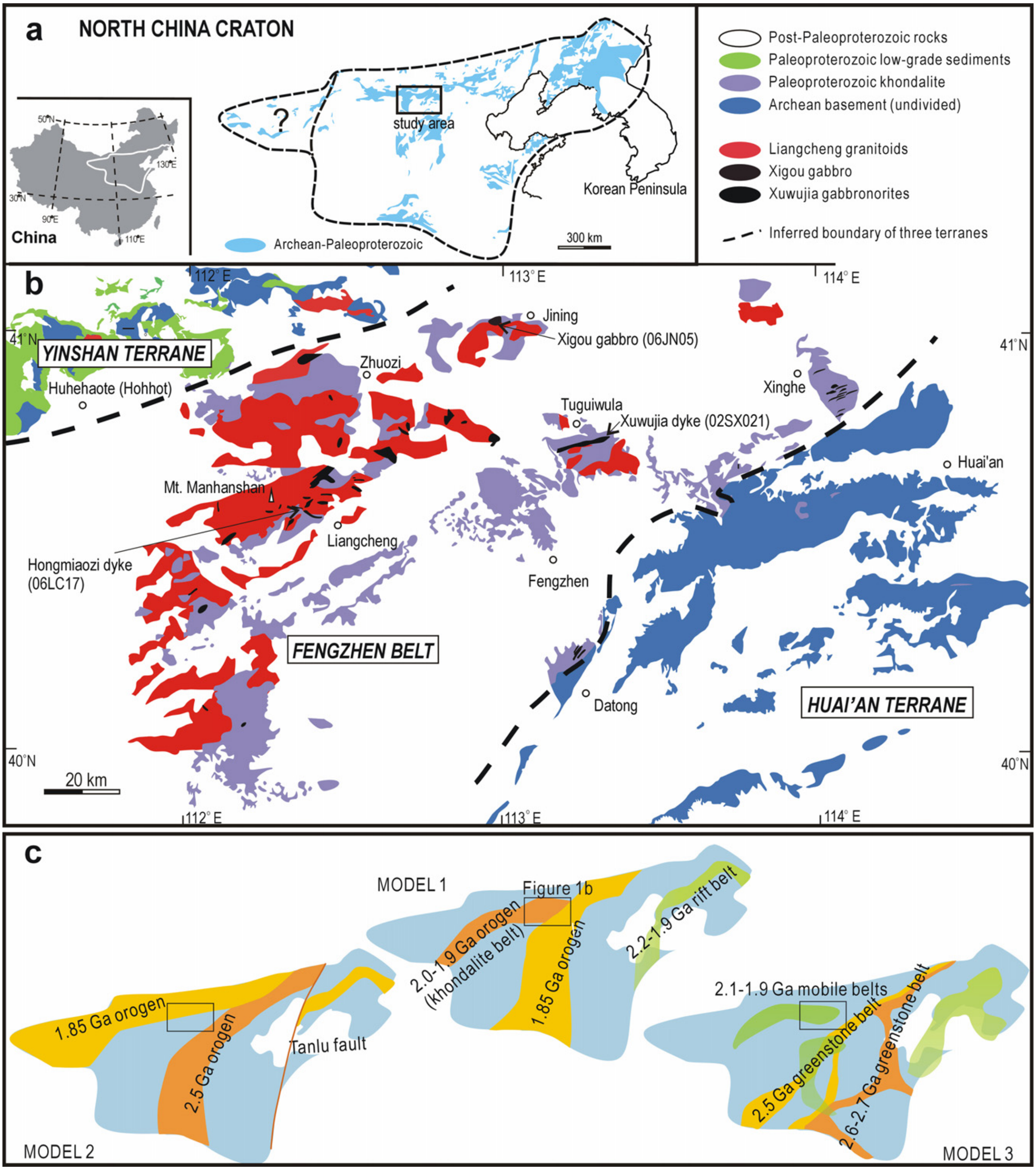

Fig. 1. Maps showing Archean-Paleoproterozoic outcrops of the North China craton (a), the Xuwujia gabbronorites, Liangcheng granitoids, and Xigou gabbro in the study area (b), and tectonic evolution models for the NCC (c, see text). TTG refers to tonalite–trondhjemite–granodiorite.

anatexis and re-melting of continental crust may lead to mingling and/or mixing of melts from mantle and crust (e.g., Cole et al., 2001; Kuşcu and Floyd, 2001; Arvin et al., 2004). In such a scenario, it would be difficult to determine the primary composition of ancient mantle-derived rocks; nevertheless this is important as primary compositions could provide essential information on the origin of magmatism. The primary MgO concentration is especially important for source region characteristics, for instance, melting temperature and pressure (e.g., Albarède, 1992), the primary eruption temperature (anhydrous olivine liquidus temperature at 1 atm calculated for the primary magma, e.g., Beattie, 1993a), and the mantle potential temperature (a temperature at which the solid mantle would adiabatically reach the surface metastably without melting, e.g., Herzberg and O'Hara, 2002). This paper deals with a suite of Paleoproterozoic gabbronorites in the northern margin of the North China craton (Fig. 1), whose emplacement was accompanied by extensive crustal anatexis and which could be derived from a mantle source region with extremely high potential temperature.

2. Geological background

2.1. Formation of the North China craton

Although it is well known that the North China craton (NCC) was formed as a result of amalgamation of Archean blocks, there are different models on this issue. Some have suggested that the NCC was formed as a result of a ca. 1.85 Ga collision between two blocks along a high-pressure metamorphic belt through the central part of the NCC: a western block previously amalgamated from two sub-blocks along a khondalite belt[1] between 2.0 and 1.9 Ga, and an eastern block that had witnessed the opening and closing of a rift between 2.2 and 1.9 Ga (Fig. 1c: Zhao et al., 1998, 2001, 2005; Wilde et al., 2002; Guo et al., 2005; Kröner et al., 2005; Liu et al., 2005). Others have suggested that the NCC amalgamated in late Archean time (ca. 2.5 Ga), followed by subduction and collision along the north margin during the late Paleoproterozoic (ca. 1.85 Ga) (Fig. 1c: Li et al., 2000, 2002; Kusky et al., 2001, 2007; Kusky and Li, 2003). Yet others have proposed that the NCC was cratonized following 2.7–2.5 Ga amalgamation of several Archean nuclei along greenstone belts; this was followed by reworking within a number of mobile belts during 2.2–1.9 Ga (Fig. 1c: Zhai and Liu, 2003; Zhai et al., 2005; Zhai and Peng, 2007). Despite these differences of opinion, it is widely accepted that the NCC was rigid by 1.78 Ga as at this time it was crosscut by a giant mafic dyke swarm, named the Taihang-Lvliang swarm (e.g., Peng et al., 2007, 2008).

2.2. Geological background for the study area

The study area (Fig. 1a and b) is located in the northern margin of the NCC, and is composed of three different units, i.e. Huai'an terrane, Fengzhen (khondalite) belt and Yinshan terrane, juxtaposed from southeast to northwest (Fig. 1). The Huai'an terrane is dominated by ca. 2.5 Ga tonalite–trondhjemite–granodiorite (TTG) gneisses with some Paleoproterozoic mafic dykes that have undergone ca. 1.85 Ga high-pressure granulite facies metamorphism, and 2.0–1.9 Ga high-potassium granitoids, in an area formerly called the Sanggan structure zone (Zhai et al., 1992; Zhao et al., 1998, 2008; Guo et al., 1999; Peng et al., 2005; Liu et al., 2009a). The Yinshan terrane is composed of ca. 2.5 Ga late Archean TTG gneisses and granulite, and a granite–greenstone belt (e.g., Zhao et al., 2005), covered by Paleoproterozoic sediments (Wan et al., 2009).

The Fengzhen (khondalite) belt is dominated by aluminous metasedimentary rocks with some granitoid and gabbronoritic intrusions that are the focus of this paper (Fig. 1b). There are also some carbonatite dykes and veins, dated at 1951 ± 5 Ma (SHRIMP U–Pb zircon age) and thought to be the product of anatexis of impure marble in the khondalite (Wan et al., 2008). These are composed of calcite plus feldspar, quartz, clinopyroxene, orthopyroxene, phlogopite, garnet and hornblende, and vary in width from ten centimeters to several meters and in length up to several hundred meters, with an E–W orientation. The khondalite is composed of sillimanite-garnet gneiss, quartz-garnet gneiss, quartz-feldspar gneiss, and marbles, interpreted to represent an original assemblage of pelites, sandstones and carbonates (Lu et al., 1996; Qian and Li, 1999), and which experienced high-grade metamorphism (8.0–10.0 kbar and 750–800 °C; clockwise P–T path) (Zhao et al., 1999). Locally, ultra-high-temperature metamorphic conditions ($T > 1000$ °C and $P > 10.0$ kbar) are preserved in some of the metasediments, and this event was dated at ca. 1.93–1.92 Ga (Santosh et al., 2006, 2007a,b; Guo et al., 2006; Liu et al., 2009b). Wan et al. (2008) and Yin et al. (2008) have distinguished another high-grade metamorphic event at 1.96–1.95 Ga that predates the ca. 1.95 Ga carbonatite dykes. This ca. 1.95 Ga magmatic event (carbonatite dykes) and metamorphic event give similar ages within error, and thus could be broadly related events. Yin et al. (2008) interpreted this metamorphism as a possible collision event.

Although the depositional age of the khondalite is controversial (e.g., Wu et al., 1997; Guo et al., 2001; Wan et al., 2006; Xia et al., 2006, 2008), two constraints are clear: (1) the khondalite is cut by granitoids with ages between ca. 1.93–1.89 Ga (Zhong et al., 2007; Guo et al., 2001) and locally some ca. 1.95 Ga carbonatite dykes (Wan et al., 2008) and (2) the youngest khondalite shows ca. 2.0 Ga detrital zircons with clear magmatic zoning (e.g., Wan et al., 2006; Xia et al., 2006). Thus we think that the depositional age for the youngest khondalite should be between 2.0 and 1.95 Ga. Study of detrital zircons and whole-rock isotopes reveal that the protoliths of the khondalite were not derived from the late Archean rocks south or north of the khondalite belt, but rather from a Paleoproterozoic crust (e.g., Xia et al., 2006, 2008), suggesting a possible "juvenile" continent or an arc. A possible Paleoproterozoic protolith of the khondalite could be ca. 2.0 Ga granites reported by Guo et al. (2001) from the northwest part of the study area, but these are as yet poorly known (Fig. 1b).

Our study area has importance with respect to the tectonic subdivision and formation models of the NCC, i.e. each model in Fig. 1c has its own interpretation for the three units (Huai'an terrane, Fengzhen belt and Yinshan terrane). In model 1, the Huai'an terrane is considered as a 2.5 Ga arc complex in a 1.85 Ga orogenic belt, the Fengzhen belt is a 1.9–2.0 Ga orogen, and the Yinshan is a late Archean continental block (Zhao et al., 2005, 2008). In model 2, the Fengzhen belt and Yinshan terrane is suggested to be an uplifted plateau due to a late Paleoproterozoic collision along the north margin, whereas the Huai'an terrane recorded a 2.5 Ga orogen in the central NCC (Kusky and Li, 2003; Kusky et al., 2007). In model 3, however, the three terranes are proposed as uplifted Archean lower crust, in which the Fengzhen belt is a 2.1–1.9 Ga mobile belt (Zhai et al., 1992; Zhai and Liu, 2003; Zhai and Peng, 2007).

3. Field relationships in the study area

The gabbronorites are preserved as numerous dykes, sills and small plutons in the khondalite and adjacent rocks, and as hundreds of entrained bodies and fragments and numberless "pillows" in the granitoids (mainly in the southeast); there are also "blobs" of hybrid granitic materials in the gabbronorites (Figs. 1 and 2). We refer to them as the Xuwujia gabbronorites, named after a village where the longest gabbronorite dyke is exposed (width ∼1–2 km, outcrop length ∼15 km). This large Xuwujia dyke is also known for its chemical variations (Peng et al., 2005). The gabbronorite intrusives generally have widths of several meters to hundreds of meters, and lengths up to several kilometers. The rocks are typically composed of orthopyroxene (hypersthene), clinopyroxene, hornblende, and plagioclase, with or without K-feldspar, and olivine or quartz. Magmatic textures are preserved, although locally they are overprinted by metamorphic features and deformational fabrics. An important observation is that gabbronoritic dykes always accompany the ultra-high-temperature metasedimentary gneisses (Fig. 2, e.g., locations in Dongpo, Xuwujia, and Tuguiwula; Guo et al., 2006, submitted for publication).

The Liangcheng granitoids are peraluminous and distributed mainly in a north-east trending belt, both north and south margins bounded by ductile shear zones (e.g., Zhai et al., 2003); a few bodies

[1] The khondalite belt refers to a tectonic unit along the western part of the northern margin of the North China craton (Fig. 1c), named for its dominant rock type, khondalite, which is a regional rock name rooted in the history of petrological research in the Indian subcontinent and refers to quartz-feldspar-sillimanite paragneisses with graphite, garnet, biotite, and/or cordierite (e.g., Condie et al., 1992).

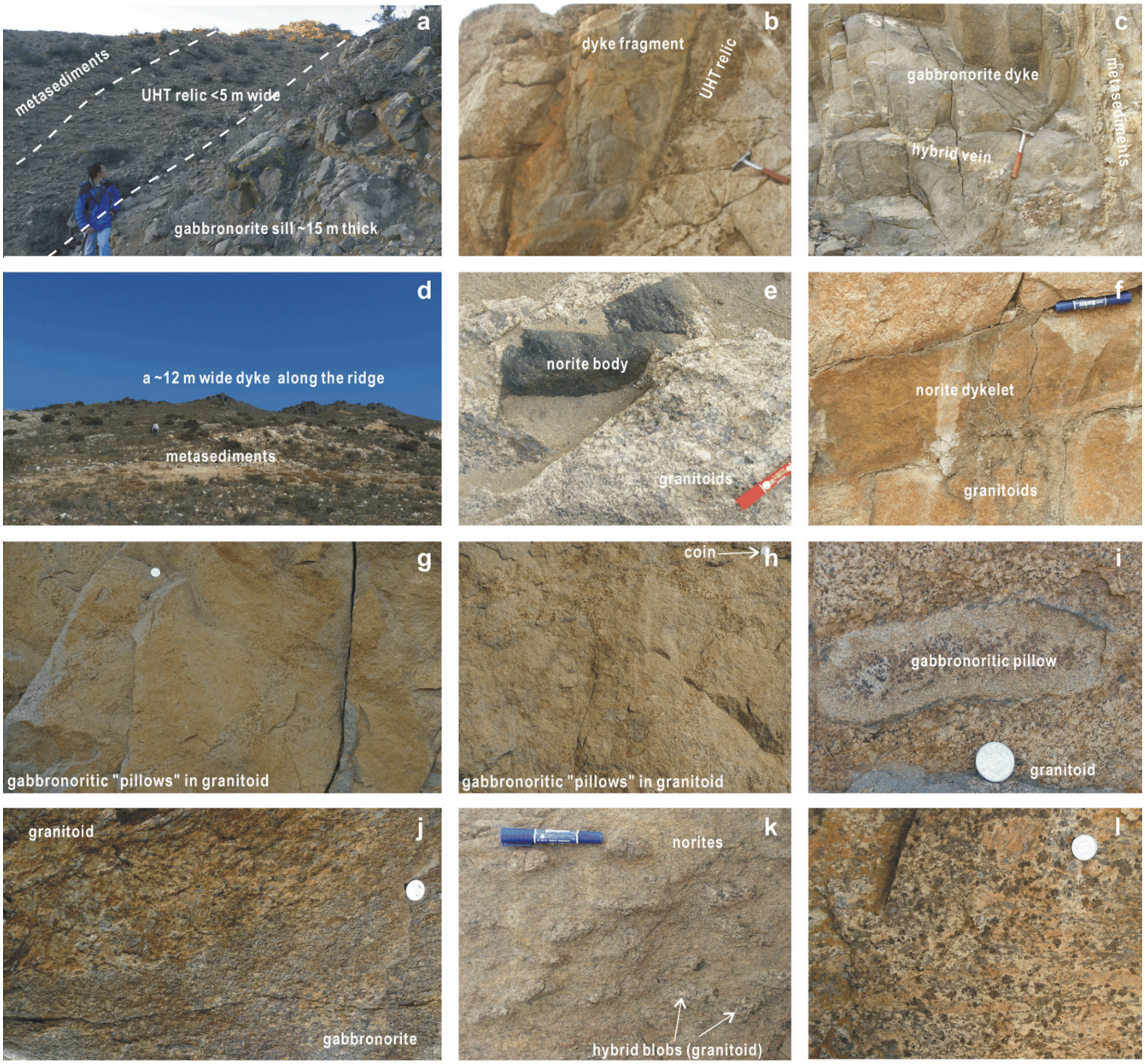

Fig. 2. Field photos of the study area: (a) UHT (ultra-high-temperature) metamorphic relic and a ~10–15 m wide gabbronorite dyke; (b) UHT relic beside a dyke fragment; (c) a gabbronoritic dyke with hybrid veins; (d) a ~15 m noritic dyke in the metasediments (khondalite) along the ridges of the hills; (e) a noritic body in the late phase of Liangcheng granitoids; (f) a small noritic dyke in Liangcheng granitoids; (g and h) gabbronoritic "pillows" in Liangcheng granitoids; (i) a noritic "pillow" in the Liangcheng granitoids; (j) transitional boundary between a gabbronorite stock and the Liangcheng granitoids; (k) blobs of hybrid materials (granitoids) in the noritic intrusion; and (l) Liangcheng granitoids with big feldspar phenocrysts. A person is shown for scale in (a) and (d); a hammer, ~40 cm long, in (b) and (c); a pen ~14 cm long in (e), (f), and (k); and a coin, ~2.5 cm in diameter, in (g)–(j) and (l).

lie outside of this belt. This belt has an approximate width of 100 km and a length of 250 km, in which the biggest granitoid intrusion is centered near Mt. Manhanshan (Fig. 1). The granitoids are composed of plagioclase, K-feldspar, garnet, quartz, and minor amounts of hypersthene and clinopyroxene. Feldspars and some of the garnets are idiomorphic. The Liangcheng granitoids are thought to be S-type granites derived from the khondalite (country rock) (e.g., Shi, 1997; Zhong et al., 2006; Guo et al., submitted for publication). Two types of garnet grains are reported in the granitoids: large crystals inherited from the khondalite; and smaller ones that were newly formed from the melts (Lan, 2006). U–Pb zircon ages ranging from ca. 1.93–1.89 Ga have been obtained for the Liangcheng granitoids (e.g., Zhong et al., 2007; Guo et al., 2001).

In the northern part of the study area, the khondalite is intruded by the Xigou gabbro. On its southwest flank, this body is in turn crosscut by Liangcheng granitoids (Fig. 1). The gabbro body is several square kilometers in size and contains magnetite-rich layers, the principal source of iron ore mineralization in this area. The gabbro shows a mineral assemblage of mainly hornblende (mostly altered from clinopyroxene with some primary relics) and plagioclase.

4. Samples and analytical methods

We collected numerous samples from the Xuwujia gabbronorites and associated rocks (Liangcheng granitoids, Xigou gabbro, and the khondalite). As most Xuwujia gabbronorites occur as deformed bodies in the khondalite or as enclaves in the Liangcheng granitoids that lack clear chilled margins, most of the Xuwujia gabbronorite samples were collected from coarse-grained and homogeneous parts, with only a few samples from finer-grained margins. The Liangcheng granitoid and the khon-

Table 1
Data of U–Pb zircon analyses for the Hongmiaozi dyke (Xuwujia gabbronorites) and Xigou gabbro.

Spot	U (ppm)	Th (ppm)	$^{232}Th/^{238}U$	$^{206}Pb^*$ (ppm)	$^{206}Pb_c$ %	$^{204}Pb/^{206}Pb$	$^{207}Pb^*/^{235}U$	$\pm\sigma$ (%)	$^{206}Pb^*/^{238}U$	$\pm\sigma$ (%)	$^{207}Pb^*/^{206}Pb^*$	$\pm\sigma$ (%)	$^{207}Pb/^{206}Pb$ age, $\pm\sigma$ (Ma)
A: SHRIMP data													
06LC17 (Hongmiaozi gabbronorite dyke)													
1	131	84	0.66	38.5	0.07	4.7E−5	5.7874	3.4	0.34119	3.0	0.12302	1.6	2001 ± 28
1.1 (rim)	43	12	0.28	11.7	0	0	5.5855	5.2	0.31478	4.1	0.12869	3.2	2080 ± 56
2.1 (rim)	44	13	0.31	11.9	0.80	5.1E−4	4.5682	5.5	0.30959	4.4	0.10702	3.4	1750 ± 62
2	105	81	0.80	30.4	0.35	2.3E−4	5.4338	4.3	0.33710	3.1	0.11691	3.0	1910 ± 54
3	124	107	0.89	37.0	0.19	1.2E−4	5.8849	3.4	0.34773	3.0	0.12274	1.7	1997 ± 29
3.1 (rim)	41	14	0.35	11.7	0	0	5.7010	4.5	0.32804	3.7	0.12605	2.7	2044 ± 47
4	87	42	0.50	25.3	0.13	8.9E−5	5.8648	5.4	0.33859	4.4	0.12563	3.0	2038 ± 53
4.1 (rim)	37	9	0.26	10.7	1.34	8.7E−4	5.2059	5.5	0.33636	3.7	0.11225	4.0	1837 ± 73
5	109	92	0.87	31.7	0.44	2.9E−4	5.4118	3.4	0.33608	3.0	0.11679	1.7	1908 ± 30
6	127	104	0.85	39.6	0.31	2.1E−4	6.3045	3.1	0.36203	2.9	0.12630	1.2	2047 ± 21
6.1 (rim)	42	11	0.27	11.7	0.90	5.8E−4	5.1122	6.1	0.32162	3.7	0.11528	4.9	1885 ± 88
7	124	96	0.80	38.9	0.06	3.9E−5	6.1394	2.7	0.36610	2.5	0.12163	1.1	1980 ± 19
7.1 (rim)	69	20	0.29	20.4	0.46	2.9E−4	5.3740	3.5	0.34410	2.6	0.11327	2.3	1853 ± 42
8	100	70	0.72	31.1	0.25	1.6E−4	5.8379	3.0	0.35959	2.8	0.11775	1.1	1922 ± 20
8.1 (rim)	34	9	0.28	10.4	1.04	6.7E−4	5.5681	4.1	0.35357	2.9	0.11422	3.0	1868 ± 54
9	108	70	0.67	32.4	0.29	1.9E−4	5.5098	2.8	0.34881	2.6	0.11456	1.2	1873 ± 23
9.1 (rim)	39	11	0.30	11.1	0.77	5.0E−4	5.3476	3.9	0.33216	2.9	0.11676	2.7	1908 ± 48
10	160	110	0.71	48.6	0.23	1.5E−4	5.7347	2.6	0.35340	2.4	0.11769	0.9	1922 ± 16
11	150	118	0.81	46.1	0	0	6.1576	2.6	0.35800	2.5	0.12475	0.8	2025 ± 14
12	111	80	0.74	32.8	0.41	2.7E−4	5.5205	2.9	0.34131	2.5	0.11731	1.5	1916 ± 26
13	74	52	0.72	22.0	0.31	2.0E−4	5.7399	3.2	0.34339	2.7	0.12123	1.7	1975 ± 30
14	91	73	0.82	27.6	0.43	2.8E−4	5.8385	3.0	0.34931	2.6	0.12122	1.6	1974 ± 28
15	170	141	0.86	50.6	0.22	1.4E−4	5.7507	2.7	0.34553	2.5	0.12071	1.0	1967 ± 18
16	125	81	0.67	37.1	0.20	1.3E−4	5.7782	2.7	0.34595	2.5	0.12114	1.1	1973 ± 19
17	135	110	0.84	40.0	0.35	2.3E−4	5.6800	2.9	0.34429	2.7	0.11965	1.2	1951 ± 21
18	282	199	0.73	84.9	0.14	9.0E−5	5.8029	2.5	0.35022	2.4	0.12017	0.7	1959 ± 12
19	182	132	0.75	54.8	0.28	1.8E−4	5.6986	2.7	0.34840	2.5	0.11863	1.0	1936 ± 18
20.1 (rim)	31	8	0.26	8.85	0.95	6.2E−4	5.1528	4.7	0.33144	3.1	0.11275	3.6	1845 ± 65
06JN05 (Xigou gabbro)													
1	3958	547	0.14	1200	0.01	4.7E−6	5.5007	2.4	0.35262	2.3	0.11314	0.38	1850 ± 7
2	7407	2102	0.29	2370	0.01	5.7E−6	5.8120	2.4	0.37281	2.4	0.11307	0.16	1849 ± 3
3	5376	618	0.12	1650	0.00	2.7E−6	5.5639	2.3	0.35618	2.3	0.11330	0.23	1853 ± 4
4	6886	519	0.08	2270	0.01	3.7E−6	6.0082	2.4	0.38372	2.4	0.11356	0.25	1857 ± 5
5	4210	596	0.15	1300	0.01	6.8E−6	5.6233	2.4	0.35860	2.3	0.11373	0.30	1860 ± 5
6	1940	412	0.22	567	0.03	2.2E−5	5.2803	2.4	0.34008	2.4	0.11261	0.43	1842 ± 8
7	7009	512	0.08	2220	0.01	4.0E−6	5.7927	2.4	0.36860	2.4	0.11398	0.25	1864 ± 5
8	7300	523	0.07	2330	0.01	4.3E−6	5.7998	2.3	0.37144	2.3	0.11324	0.24	1852 ± 4
9	6209	3057	0.51	1950	0.01	3.3E−6	5.7413	2.4	0.36559	2.4	0.11390	0.25	1863 ± 5
10	5212	453	0.09	1600	0.01	3.9E−6	5.6129	2.4	0.35661	2.4	0.11415	0.27	1867 ± 5
11	5617	426	0.08	1730	0.01	5.7E−6	5.6222	2.6	0.35833	2.6	0.11380	0.27	1861 ± 5
12	4282	767	0.18	1290	0.01	9.4E−6	5.5203	2.4	0.35090	2.3	0.11410	0.32	1866 ± 6
13	1786	138	0.08	524	0.01	3.7E−6	5.3174	2.4	0.34125	2.4	0.11301	0.48	1848 ± 9
13.1 (rim)	3103	355	0.12	862	0.05	3.2E−5	5.1299	2.4	0.32330	2.4	0.11508	0.45	1881 ± 8
14.1 (rim)	7073	1802	0.26	2230	0.01	4.3E−6	5.7426	2.4	0.36674	2.3	0.11357	0.26	1857 ± 5
15	5177	1216	0.24	1600	0.01	8.3E−6	5.6432	2.4	0.36001	2.3	0.11369	0.30	1859 ± 5

Table 1 (*Continued*)

Spot	U (ppm)	Th (ppm)	Pb (ppm)	Th/U	$^{204}Pb/^{206}Pb$	$^{207}Pb/^{235}U$	±σ %	$^{206}Pb/^{238}U$	±σ %	$^{207}Pb/^{206}Pb$	±σ %	ρ	$^{207}Pb/^{206}Pb$ age,±σ (Ma)
B: CAMECA data													
06LC17 (Hongmiaozi gabbronorite dyke)													
1	160	126	75	0.78	6.8E−06	5.8490	1.57	0.35074	1.50	0.12095	0.45	0.96	1970 ± 8
2	120	89	55	0.74	1.2E−05	5.7942	1.59	0.34809	1.50	0.12073	0.52	0.94	1967 ± 9
3 (rim)	45	14	18	0.31	2.5E−05	5.4760	1.81	0.34044	1.58	0.11666	0.88	0.87	1905 ± 16
4	109	81	49	0.74	2.6E−05	5.6337	1.71	0.34370	1.52	0.11888	0.78	0.89	1939 ± 14
5	133	106	63	0.79	5.5E−06	5.8588	1.65	0.35406	1.50	0.12001	0.67	0.91	1956 ± 12
6	107	56	47	0.52	1.4E−05	5.8141	1.64	0.34902	1.54	0.12082	0.56	0.94	1968 ± 10
7 (rim)	78	33	32	0.42	1.4E−05	5.5511	1.64	0.33982	1.50	0.11848	0.66	0.92	1933 ± 12
8	26	8	11	0.30	8.1E−05	5.6854	1.96	0.34065	1.50	0.12105	1.25	0.77	1971 ± 22
9 (rim)	37	10	15	0.27	3.3E−06	5.7063	1.77	0.34930	1.50	0.11848	0.95	0.85	1933 ± 17
10 (rim)	73	25	30	0.34	2.9E−05	5.4583	1.66	0.33895	1.50	0.11679	0.69	0.91	1907 ± 12
11	56	28	24	0.51	1.3E−05	5.7053	1.69	0.34498	1.50	0.11995	0.77	0.89	1955 ± 14
12 (rim)	77	34	33	0.44	2.7E−05	5.6623	1.65	0.34849	1.51	0.11784	0.68	0.91	1923 ± 12
13 (rim)	40	11	17	0.28	6.9E−05	5.6652	1.78	0.34804	1.50	0.11806	0.95	0.85	1927 ± 17
14	226	172	105	0.76	7.8E−06	5.8040	1.55	0.35053	1.50	0.12009	0.38	0.97	1957 ± 7
15 (rim)	33	8	14	0.25	3.2E−05	5.6642	2.47	0.34728	1.50	0.11830	1.96	0.61	1930 ± 15
16 (rim)	92	33	39	0.37	2.3E−05	5.6452	1.63	0.34654	1.51	0.11815	0.61	0.93	1928 ± 11
17	245	166	113	0.68	4.3E−06	5.9121	1.59	0.35556	1.51	0.12060	0.50	0.95	1965 ± 9
18 (rim)	67	36	29	0.54	2.6E−05	5.6142	1.66	0.34646	1.50	0.11753	0.72	0.90	1918 ± 12
19	35	11	15	0.33	1.1E−05	5.8432	1.79	0.35250	1.50	0.12022	0.97	0.84	1959 ± 17
20	69	44	31	0.64	1.1E−05	5.7222	1.65	0.34498	1.50	0.12030	0.69	0.91	1960 ± 12
21	167	130	79	0.78	1.5E−05	5.8962	1.72	0.35524	1.52	0.12038	0.81	0.88	1961 ± 14
22 (rim)	38	13	15	0.33	1.1E−05	5.4983	1.82	0.33667	1.50	0.11845	1.02	0.83	1932 ± 18
23	126	87	57	0.69	0	5.7972	1.72	0.34958	1.52	0.12027	0.81	0.88	1960 ± 14
24 (rim)	37	10	15	0.26	1.1E−05	5.5043	1.78	0.33807	1.50	0.11808	0.95	0.85	1927 ± 17
25	146	125	68	0.86	1.4E−05	5.5245	1.58	0.34235	1.50	0.11704	0.48	0.95	1911 ± 9
26 (rim)	34	9	14	0.27	6.0E−05	5.5633	1.83	0.34671	1.50	0.11638	1.04	0.82	1901 ± 19
27 (rim)	31	9	12	0.30	4.7E−05	5.5430	1.88	0.33996	1.50	0.11826	1.13	0.80	1930 ± 20
28	125	102	58	0.82	3.0E−05	5.7177	1.59	0.34825	1.50	0.11908	0.52	0.94	1942 ± 9
29	126	101	58	0.80	3.0E−05	5.6726	1.90	0.34211	1.50	0.12026	1.16	0.79	1960 ± 21
30	154	117	72	0.76	1.8E−05	5.8492	1.61	0.35238	1.54	0.12039	0.50	0.95	1962 ± 9
31	105	69	48	0.66	6.3E−05	5.9079	1.73	0.35433	1.51	0.12093	0.84	0.87	1970 ± 15
32	95	33	40	0.35	8.2E−06	5.7333	1.61	0.34924	1.50	0.11906	0.59	0.93	1942 ± 11
33	210	167	99	0.79	1.3E−05	5.8902	1.56	0.35464	1.50	0.12046	0.40	0.97	1963 ± 7
34	115	93	53	0.81	1.6E−05	5.6641	1.60	0.34578	1.50	0.11880	0.55	0.94	1938 ± 10
35	136	105	64	0.78	0	5.8566	1.66	0.35340	1.50	0.12019	0.70	0.91	1959 ± 12
36	226	171	106	0.75	4.9E−06	5.8547	1.55	0.35326	1.50	0.12020	0.39	0.97	1959 ± 7
37	118	81	53	0.68	3.5E−06	5.7463	1.76	0.34775	1.55	0.11984	0.83	0.88	1953 ± 15
38 (rim)	37	11	16	0.28	3.2E−05	5.7739	1.80	0.35482	1.50	0.11802	0.99	0.84	1926 ± 18
39	138	78	62	0.57	1.1E−05	5.8051	1.58	0.35168	1.50	0.11972	0.50	0.95	1952 ± 9
40	116	92	56	0.80	1.6E−05	5.9495	1.83	0.36040	1.56	0.11973	0.97	0.85	1952 ± 17

Notes: Pb_c and Pb^* indicate the common and radiogenic portions, respectively. Common Pb is corrected using measured ^{204}Pb. ρ represents error correlation coefficient.

Table 2
Lu–Hf analyses for zircon grains of the Xuwujia and Hongmiaozi dykes (Xuwujia gabbronorites) and the Xigou gabbro.

Sample	$^{176}Lu/^{177}Hf$	$^{176}Hf/^{177}Hf$ (2σ)	$^{207}Pb/^{206}Pb$ age, Ma	$^{176}Hf/^{177}Hf_i$	εHf_{t1}	εHf_{t2}	T_{DM} (Ma)	$f_{Lu/Hf}$
02SX021 (Xuwujia gabbronorite dyke)								
−4	0.001093	0.281562 ± 15	1904	0.281523	−1.8	−1.2	2373	−0.97
−5	0.000741	0.281615 ± 16	1920	0.281588	0.9	1.2	2279	−0.98
−7	0.000441	0.281670 ± 20	1937	0.281654	3.7	3.5	2187	−0.99
−8	0.000681	0.281652 ± 19	1920	0.281627	2.3	2.6	2224	−0.98
−9	0.000459	0.281527 ± 16	1928	0.281511	−1.6	−1.6	2381	−0.99
−10	0.000323	0.281642 ± 26	1915	0.281630	2.3	2.6	2218	−0.99
−11	0.000589	0.281583 ± 17	1948	0.281561	0.6	0.2	2314	−0.98
−12	0.000244	0.281601 ± 16	1912	0.281592	0.9	1.3	2268	−0.99
−13	0.000533	0.281577 ± 15	1942	0.281557	0.4	0.1	2318	−0.98
−14	0.000794	0.281633 ± 16	1937	0.281604	1.9	1.7	2257	−0.98
−15	0.000314	0.281614 ± 19	1924	0.281602	1.5	1.7	2256	−0.99
06LC17 (Hongmiaozi gabbronorite dyke)								
−1	0.000492	0.281529 ± 23	2001	0.281511	0.0	−1.6	2380	−0.99
−1.1 (rim)	0.000199	0.281552 ± 24	2080	0.281544	3.0	−0.4	2331	−0.99
−2	0.000416	0.281528 ± 19	1910	0.281513	−2.0	−1.5	2378	−0.99
−2.1 (rim)	0.000188	0.281585 ± 24	1750	0.281579	−3.3	0.8	2287	−0.99
−3	0.000732	0.281553 ± 25	1997	0.281525	0.4	−1.0	2363	−0.98
−3.1 (rim)	0.000340	0.281557 ± 24	2044	0.281544	2.2	−0.4	2334	−0.99
−4	0.000348	0.281563 ± 25	2038	0.281550	2.3	−0.2	2326	−0.99
−4.1 (rim)	0.000205	0.281540 ± 25	1837	0.281533	−2.9	−0.8	2349	−0.99
−5	0.000835	0.281537 ± 23	1908	0.281507	−2.2	−1.7	2391	−0.97
−6	0.000541	0.281536 ± 20	2047	0.281515	1.3	−1.4	2374	−0.98
−6.1 (rim)	0.000225	0.281530 ± 24	1885	0.281522	−2.2	−1.2	2364	−0.99
−7	0.000718	0.281558 ± 21	1980	0.281531	0.3	−0.8	2355	−0.98
−7.1 (rim)	0.000257	0.281552 ± 17	1853	0.281543	−2.2	−0.4	2335	−0.99
−8	0.000506	0.281513 ± 21	1922	0.281494	−2.3	−2.2	2404	−0.98
−8.1 (rim)	0.000268	0.281545 ± 19	1868	0.281535	−2.1	−0.7	2346	−0.99
−9	0.000611	0.281611 ± 21	1873	0.281589	−0.1	1.2	2277	−0.98
−9.1 (rim)	0.000199	0.281536 ± 19	1908	0.281529	−1.5	−0.9	2354	−0.99
−10	0.000480	0.281541 ± 17	1922	0.281524	−1.3	−1.1	2363	−0.99
−11	0.000833	0.281652 ± 21	2025	0.281620	4.5	2.4	2233	−0.97
−13	0.000412	0.281511 ± 21	1975	0.281496	−1.1	−2.1	2400	−0.99
−14	0.000564	0.281578 ± 27	1974	0.281556	1.1	0.1	2319	−0.98
−15	0.000527	0.281512 ± 22	1967	0.281492	−1.4	−2.2	2406	−0.98
−16	0.000273	0.281484 ± 18	1973	0.281473	−1.9	−2.9	2428	−0.99
−18	0.000832	0.281529 ± 20	1959	0.281498	−1.4	−2.0	2402	−0.97
−19	0.000733	0.281513 ± 22	1936	0.281486	−2.3	−2.5	2418	−0.98
−20.1 (rim)	0.000235	0.281531 ± 19	1845	0.281523	−3.1	−1.2	2362	−0.99
06JN05 (Xigou gabbro)								
−1	0.000779	0.281435 ± 17	1850	0.281408	−7.0	−5.3	2526	−0.98
−2	0.001290	0.281482 ± 24	1849	0.281437	−6.0	−4.3	2495	−0.96
−3	0.000496	0.281455 ± 23	1853	0.281438	−5.9	−4.2	2481	−0.99
−4	0.000753	0.281461 ± 16	1857	0.281434	−6.0	−4.3	2490	−0.98
−5	0.000784	0.281475 ± 21	1860	0.281447	−5.4	−3.9	2473	−0.98
−6	0.000316	0.281515 ± 28	1842	0.281504	−3.8	−1.9	2389	−0.99
−7	0.000745	0.281503 ± 18	1864	0.281476	−4.3	−2.8	2432	−0.98
−8	0.000773	0.281485 ± 15	1852	0.281458	−5.2	−3.5	2458	−0.98
−10	0.000726	0.281483 ± 18	1867	0.281457	−4.9	−3.5	2458	−0.98
−11	0.000789	0.281481 ± 18	1861	0.281454	−5.2	−3.6	2464	−0.98
−12	0.000732	0.281425 ± 19	1866	0.281399	−7.0	−5.6	2537	−0.98
−13	0.000531	0.281483 ± 28	1848	0.281465	−5.1	−3.3	2445	−0.98
−13.1 (rim)	0.001059	0.281461 ± 26	1881	0.281424	−5.8	−4.7	2509	−0.97
−14	0.000925	0.281458 ± 21	1857	0.281425	−6.3	−4.7	2505	−0.97
−15	0.001169	0.281471 ± 20	1859	0.281430	−6.1	−4.5	2503	−0.96

Notes: $\varepsilon Hf_t = 10000 \times \{[(^{176}Hf/^{177}Hf)_{sample} - (^{176}Lu/^{177}Hf)_{sample} \times (e^{\lambda t} - 1)]/[(^{176}Hf/^{177}Hf)_{CHUR} - (^{176}Lu/^{177}Hf)_{CHUR} \times (e^{\lambda t} - 1)] - 1\}$. $T_{DM} = 1/\lambda \times \ln\{1 + [(^{176}Hf/^{177}Hf)_{sample} - (^{176}Hf/^{177}Hf)_{DM}]/[(^{176}Lu/^{177}Hf)_{sample} - (^{176}Lu/^{177}Hf)_{DM}]\}$. $f_{Lu/Hf} = (^{176}Lu/^{177}Hf)_{Sample}/(^{176}Lu/^{177}Hf)_{CHUR} - 1$. The $^{176}Hf/^{177}Hf$ and $^{176}Lu/^{177}Hf$ ratios of chondrite (CHUR) and depleted mantle (DM) at the present day are 0.282772 and 0.0332, and 0.28325 and 0.0384, respectively (Blichert-Toft and Albarède, 1997; Griffin et al., 2000). $\lambda = 1.867 \times 10^{-11}$ A^{-1} (Söderlund et al., 2004). εHf_{t1} is calculated using the SHRIMP $^{207}Pb/^{206}Pb$ age of each spot, and εHf_{t2} is calculated to 1930 Ma.

dalite samples are all from homogeneous rocks, while the Xigou gabbro samples are from representative gabbroic parts of this body.

Zircon U–Pb and Lu–Hf analyses, and bulk whole-rock major and trace element and Sr–Nd isotopic analyses were performed on selected samples (Tables 1–5). Except for the SHRIMP zircon U–Pb analyses, which were done at the Beijing SHRIMP Center, all other analyses were performed in the State Key Laboratory of Lithospheric Evolution, Chinese Academy of Sciences, Beijing. Zircon grains were separated using standard heavy liquid and magnetic techniques, and were selected and mounted in an epoxy resin together with standard Temora 1 zircons (conventional ID-TIMS $^{206}Pb/^{238}U$ age = 417 Ma, Black et al., 2003). The mount was polished to expose the centers of the grains, and then gold coated. Optical microscope images were taken to obtain information on the shapes of the grains and their positions in the mount. Cathodoluminescence and backscattered electron images were acquired, using a scanning electron microscope at the Beijing SHRIMP Center in order to examine their internal structures.

Zircon U–Pb isotope analyses (Table 1) were carried out using both CAMECA IMS 1280 and SHRIMP-II instruments. The diameter of the analytical ion beam at the sample surface was approximately 30–40 μm with the SHRIMP and ∼20 μm with the CAMECA ion probe. For both methods, common Pb was corrected using the measured ^{204}Pb. All data were processed using the Squid 1.02 and

Table 3
Selected whole-rock major element data (wt.%) and calculated norms for the Xuwujia gabbronorites and associated rocks.

Sample	Group																				
	Xuwujia gabbronorites (high-Mg group)												Xuwujia gabbronorites (low-Mg group)								
	99XBY-4	99XBY5-1	99XBY5-2	99XBY6-1	99XBY6-2	99XBY6-4	99XBY-8	07XBY02	99XBY6-3	07XBY08	99XW-3	99XW-7	06LC07	06LC17	99XW9	99LC1	99LC2	99LC3	99LC4	99LC5	99LC6
SiO_2	50.3	47.6	46.7	46.4	45.4	46.7	47.2	49.2	46.9	50.6	48.0	50.1	53.8	49.6	49.5	54.2	54.3	54.5	55.1	55.4	49.8
TiO_2	0.42	0.62	0.75	1.02	0.52	0.90	0.57	0.34	0.42	0.39	0.63	0.42	1.56	2.68	1.36	1.62	1.85	2.50	1.70	1.37	3.05
Al_2O_3	6.61	16.77	13.46	18.81	12.39	17.95	8.93	8.79	8.82	8.02	13.94	9.45	15.42	15.45	18.12	19.28	19.14	17.24	18.00	19.05	15.02
Fe_2O_3t	12.9	9.8	11.9	12.1	13.6	12.6	13.1	10.9	8.9	12.2	11.8	10.6	13.5	13.8	9.7	10.3	10.0	10.2	10.7	9.5	15.8
MnO	0.26	0.18	0.21	0.21	0.23	0.21	0.23	0.14	0.18	0.19	0.24	0.24	0.19	0.18	0.16	0.15	0.16	0.17	0.16	0.15	0.21
MgO	19.00	12.00	13.30	7.10	17.80	6.20	18.10	22.85	13.30	19.33	9.73	18.32	4.43	5.49	5.39	2.70	2.72	2.50	2.60	2.20	4.30
CaO	7.30	9.60	9.62	11.10	6.80	10.70	7.40	6.03	16.90	7.90	10.33	7.63	8.10	8.27	8.47	5.20	5.30	5.32	5.30	4.90	5.20
Na_2O	0.44	0.96	0.94	1.21	0.50	1.08	0.57	0.92	0.47	0.69	0.86	0.37	1.83	2.69	2.73	2.64	2.67	2.65	2.63	3.00	1.83
K_2O	0.19	0.38	0.39	0.19	0.26	0.10	0.34	0.48	0.64	0.50	1.37	0.85	1.25	0.95	1.36	1.59	1.71	1.83	1.68	1.99	1.57
P_2O_5	0	0	0.20	0.23	0	0.01	0.01	0.05	0	0.04	0.08	0.09	0.21	1.17	0.69	0.57	0.73	1.10	0.67	0.63	1.23
LOI	0.35	0.40	0.66	0.47	1.00	1.10	1.40	0.30	0.50	0.08	2.93	1.92	-0.60	-0.03	2.26	1.20	1.10	1.30	1.10	1.30	1.20
Total	97.8	98.3	98.1	98.8	98.5	97.6	97.9	100.0	97.0	99.9	99.9	100.0	99.7	100.3	99.7	99.5	99.7	99.3	99.6	99.5	99.2
Mg#	75	72	71	56	74	51	75	82	76	77	64	79	44	48	57	38	39	37	36	35	39
Q	0	0	0	0.2	0	3.1	0	0	0	0	0	0	10.1	2.7	0.3	14.5	14.4	16.0	15.1	13.9	12.0
Or	1.2	2.3	2.4	1.2	1.6	0.6	2.1	2.9	4.0	3.0	8.5	5.2	7.5	5.7	8.3	9.7	10.4	11.1	10.2	12.1	9.6
Ab	3.9	8.4	8.2	10.5	4.4	9.6	5.1	7.9	3.9	5.9	7.6	3.2	15.6	23.0	23.9	22.9	23.1	23.1	22.8	26.0	16.0
An	16.1	41.5	32.5	46.5	31.9	45.9	21.8	18.7	20.9	17.5	31.4	22.2	30.4	27.5	34.3	23.1	22.5	20.5	22.9	21.2	19.2
Ne	0	0	0	0	0	0	0	0	0.1	0	0	0	0	0	0	0	0	0	0	0	0
C	0	0	0	0	0	0	0	0	0	0	0	0	0	0	0	5.1	4.9	3.7	3.7	4.5	3.6
Di	17.3	6.1	12.7	7.1	2.5	8.0	13.4	9.0	53.4	17.6	17.6	13.0	7.5	5.8	4.1	0	0	0	0	0	0
Hy	57.8	33.5	30	29.3	37.1	28.0	41.9	36.0	0	43.7	28.5	48.9	22.6	24.6	22.8	18.0	17.2	15.9	18.1	16.1	27.2
Ol	0.1	4.8	9.5	0	18.4	0	11.6	22.4	14.9	8.9	2.5	4.2	0	0	0	0	0	0	0	0	0
Mt	2.9	2.2	2.7	2.7	3.1	2.9	3.0	2.4	2.0	2.7	2.7	2.4	3.0	3.0	2.2	2.3	2.2	2.3	2.4	2.1	3.6
Il	0.8	1.2	1.5	2.0	1.0	1.8	1.1	0.7	0.8	0.8	1.3	0.8	3.0	5.1	2.7	3.2	3.6	4.9	3.3	2.7	6.0
Ap	0	0	0.5	0.5	0	0	0	0.1	0	0.1	0.2	0.2	0.5	2.6	1.6	1.3	1.6	2.5	1.5	1.4	2.8

Table 3 (*Continued*)

Sample	Group																				
	Xuwujia gabbronorites (low-Mg group)														Xigou gabbro						
	99LC7	99LC20	99XW5	03JN03	99XW1-1	99XW1-2	99XW6	06LC13	02SX021	06LC01	99LC15	99LC16-1	99LC18	99LC21	06JN03	06JN05	06JN06	99JN2-1	99JN2-2	99JN2-3	99JN2-4
SiO_2	48.9	57.6	49.6	48.9	49.3	53.7	55.1	59.7	55.0	57.9	57.8	59.0	58.6	58.4	51.1	50.1	49.0	46.2	51.0	48.8	48.9
TiO_2	3.20	1.34	1.64	1.59	1.62	1.09	1.81	1.24	1.47	1.34	1.29	1.28	1.26	0.98	0.34	0.35	0.35	0.48	0.31	0.38	0.31
Al_2O_3	14.88	16.58	18.14	17.28	18.20	17.61	16.59	16.02	17.27	16.35	16.60	17.17	16.48	17.58	15.62	16.52	17.00	15.92	17.80	16.52	16.60
Fe_2O_3t	15.0	8.6	10.5	11.3	10.4	9.2	9.4	8.4	9.9	9.1	8.1	7.4	8.3	6.8	8.0	6.7	6.6	11.6	7.3	8.0	6.9
MnO	0.23	0.16	0.19	0.13	0.14	0.18	0.14	0.08	0.12	0.11	0.15	0.13	0.14	0.12	0.15	0.12	0.12	0.21	0.18	0.17	0.18
MgO	4.90	3.23	5.26	5.71	4.78	5.06	2.87	2.95	4.15	3.70	3.23	3.07	3.10	2.85	10.11	8.90	8.74	8.10	7.51	8.82	8.40
CaO	5.80	5.50	7.65	8.61	7.55	7.47	5.53	4.91	6.84	5.28	5.31	5.30	5.13	5.03	11.81	11.60	11.25	11.41	11.92	12.50	11.88
Na_2O	1.85	3.06	3.04	3.00	3.05	3.21	2.83	3.08	2.35	2.85	2.68	2.32	2.76	2.79	2.39	2.67	2.55	2.76	2.47	2.06	2.90
K_2O	1.59	2.05	1.57	1.15	1.76	0.72	3.23	1.82	0.68	2.21	2.54	2.32	2.39	2.87	0.25	0.82	1.44	0.82	0.31	0.36	0.69
P_2O_5	1.63	0.48	0.70	0.93	0.86	0.27	0.95	0.25	0.63	0.45	0.46	0.41	0.40	0.39	0.04	0.04	0.05	0.01	0.05	0.08	0.04
LOI	0.89	1.10	1.45	1.02	1.91	1.44	1.42	0.43	0.68	−0.45	1.23	0.98	1.05	1.56	−0.07	1.27	1.61	2.06	1.18	1.83	2.86
Total	98.9	99.7	99.7	99.6	99.6	100.0	99.9	98.9	99.1	98.8	99.4	99.4	99.6	99.4	99.7	99.1	98.7	99.6	100.0	99.5	99.7
Mg#	43	47	54	54	52	56	42	45	50	49	48	49	47	50	75	76	76	62	71	72	74
Q	10.3	12.7	0	0	0	21.9	8.5	16.9	15.1	12.9	13.9	18.7	15.1	14.2	0	0	0	0	0	0	0
Or	9.7	12.4	9.5	7.0	10.8	4.4	19.6	11.0	4.1	13.3	15.4	14.0	14.5	17.5	1.5	5.0	8.8	5.0	1.9	2.2	4.2
Ab	16.2	26.4	26.4	26.0	26.6	27.8	24.5	26.6	20.4	24.5	23.2	20.1	23.9	24.3	20.4	23.2	20.1	15.7	21.3	18.0	22.8
An	19.9	25.0	32.0	31.0	31.8	4.3	22.4	23.4	31.0	23.9	24.3	24.4	23.6	23.3	31.4	31.5	31.7	29.6	37.2	35.8	31.4
Ne	0	0	0	0	0	0	0	0	0	0	0	0	0	0	0	0	1.2	4.6	0	0	1.5
C	3.2	0.4	0	0	0	0	0.4	0.6	1.6	0.6	0.8	2.1	0.9	1.6	0	0	0	0	0	0	0
Di	0	0	2.3	5.9	1.5	26.3	0	0	0	0	0	0	0	0	22.1	22.0	20.7	23.7	18.4	22.3	23.9
Hy	27.5	17.5	19.8	17.9	19.5	10.6	16.9	16.6	21.3	19.2	17.1	15.7	16.9	14.9	15.1	4.0	0	0	17.4	10.8	0
Ol	0	0	2.9	4.5	2.5	0	0	0	0	0	0	0	0	0	7.1	12.0	15.1	17.7	1.5	8.2	14.0
Mt	3.4	1.9	2.3	2.5	2.3	2.1	2.1	1.9	2.2	2.0	1.8	1.7	1.8	1.5	1.8	1.5	1.5	2.6	1.6	1.8	1.6
Il	6.3	2.6	3.2	3.1	3.2	2.1	3.5	2.4	2.9	2.6	2.5	2.5	2.5	1.9	0.7	0.7	0.7	1.0	0.6	0.7	0.6
Ap	3.7	1.1	1.6	2.1	1.9	0.6	2.1	0.6	1.4	1.0	1.0	0.9	0.9	0.9	0.1	0.1	0.1	0	0.1	0.2	0.1

Table 3 (*Continued*)

Sample	Group																				
	Xigou gabbro		Liangcheng granitoids																		Khondalite
	99JN4	99JN5	99JN2-5	06LC27	06ZZ01	06LC01	06LC09	06LC10	06LC15	06LC21	06LC25	06TG01	06ZZ02	BSH-6	BSH-5-2	TG402	HL401	HL402-1	HL402-2	HL403-2	02SX008
SiO_2	50.0	50.7	48.6	63.3	65.1	66.2	61.0	64.0	61.7	73.3	71.8	61.1	62.4	61.6	62.5	61.6	66.7	65.7	65.3	74.5	75.3
TiO_2	0.35	0.36	0.34	1.21	1.13	1.02	0.82	0.54	1.09	0.17	0.28	0.84	0.93	1.16	0.97	1.02	0.51	0.82	0.88	0.66	0.02
Al_2O_3	17.49	17.11	17.05	15.81	13.79	15.63	20.50	17.88	16.88	15.15	14.69	19.38	17.53	16.48	15.92	18.10	16.27	15.75	16.30	13.45	14.21
Fe_2O_3t	6.7	6.3	6.7	6.8	7.7	7.1	9.6	4.2	8.9	1.2	2.5	9.4	7.3	8.2	8.4	5.6	6.0	5.9	6.1	4.6	0.1
MnO	0.19	0.19	0.16	0.07	0.08	0.07	0.10	0.04	0.11	0.01	0.05	0.13	0.08	0.09	0.10	0.06	0.06	0.08	0.07	0.05	0
MgO	8.25	8.41	9.02	2.02	0.64	2.30	3.38	1.25	2.58	0.29	0.64	3.27	2.66	2.49	2.40	2.89	1.54	2.99	1.74	1.42	0
CaO	12.54	12.62	12.00	4.19	3.35	2.67	0.49	1.67	3.25	1.32	1.02	1.69	3.55	3.64	3.26	3.94	2.84	2.95	2.96	1.26	0.96
Na_2O	2.47	2.11	1.88	2.64	2.20	2.90	0.54	2.55	2.54	4.51	2.44	1.80	3.35	2.13	2.58	3.03	2.55	2.38	2.53	1.99	3.54
K_2O	0.26	0.27	0.97	3.72	4.60	1.25	3.17	7.10	2.21	3.48	5.79	1.88	1.68	2.98	3.00	3.01	3.25	4.07	3.72	2.56	5.47
P_2O_5	0.05	0.06	0.06	0.42	0.50	0.04	0.03	0.13	0.04	0.05	0.10	0.05	0.07	0.28	0.07	0.19	0.14	0.15	0.15	0.07	0.09
LOI	1.36	1.40	2.85	−0.45	−0.15	0.57	0.33	0.27	0.50	0.22	0.48	0	0.22	0.32	0.22	0.64	0.64	0.35	0.25	0.16	0.33
Total	99.7	99.5	99.6	99.7	98.9	99.8	100.0	99.6	99.8	99.7	99.8	99.5	99.8	99.4	99.4	100.1	100.5	101.1	100.0	100.7	100.0
Mg#	74	76	76	41	16	43	45	41	41	37	38	45	46	42	40	55	38	54	40	42	0
Q	0	0	0	19.8	24.5	32.7	35.2	15.0	23.8	30.3	31.6	30.7	21.9	21.7	23.4	17.9	28.5	22.9	25.0	46.2	31.9
Or	1.6	1.6	6.0	22.1	27.6	7.5	19.0	42.4	13.3	20.7	34.6	11.3	10	18.0	17.9	18.0	19.4	24.0	22.2	15.1	32.5
Ab	21.4	18.3	16.5	22.4	18.9	24.9	4.6	21.8	21.8	38.4	20.8	15.4	28.6	22.1	18.3	25.9	21.7	20.1	21.6	16.8	30.1
An	36.7	37.3	36.6	18.4	13.9	13.2	2.3	7.6	16.1	6.3	4.5	8.2	17.4	16.0	16.7	18.6	13.4	13.7	13.9	5.8	4.8
C	0	0	0	0.7	0.2	4.8	15.5	3.3	4.5	1.7	2.8	11.6	3.9	2.7	3.8	3.1	3.7	2.4	3.1	5.3	0.7
Di	21.5	21.3	20.1	0	0	0	0	0	0	0	0	0	0	0	0	0	0	0	0	0	0
Hy	9.8	19.2	8.7	12.0	9.9	13.1	19.5	7.6	16.0	1.9	4.3	19.0	14.4	15.6	15.2	12.9	10.8	13.8	11.0	8.4	0
Ol	6.8	0.1	9.9	0	0	0	0	0	0	0	0	0	0	0	0	0	0	0	0	0	0
Mt	1.5	1.4	1.5	1.5	1.7	1.8	2.3	1.1	2.2	0.3	0.6	2.3	1.8	1.9	1.8	1.2	1.3	1.3	1.3	1.0	0.1
Il	0.7	0.7	0.7	2.3	2.2	2.0	1.6	1.0	2.1	0.3	0.5	1.6	1.8	1.9	2.2	2.0	1.0	1.6	1.7	1.3	0
Ap	0.1	0.1	0.1	0.9	1.1	0.1	0.1	0.3	0.1	0.1	0.2	0.1	0.2	0.2	0.6	0.4	0.3	0.3	0.3	0.2	0

Notes: Fe_2O_3t: total iron. LOI: loss-on-ignition. Mg#: Mg number. Q: quartz, Or: orthoclase, Ab: albite, An: anorthite, Ne: nepheline, C: corundum, Di: diopside, Hy: hypersthene, Ol: olivine, Mt: magnetite, Il: ilmenite, Ap: apatite. Data of samples BSH-6, BSH-5-2, TG402, HL401, HL402-2 and HL403-2 are from Zhong et al. (2006).

Table 4
Selected whole-rock trace element data (ppm) of the Xuwujia gabbronorites and associated rocks.

Sample	Group																						
	Xuwujia gabbronorites (high-Mg group)									Xuwujia gabbronorites (low-Mg group)													
	99XBY-4	99XBY5-1	99XBY5-2	99XBY6-1	99XBY6-2	99XBY6-4	99XBY-8	07XBY02	99XW-3	06LC07	06LC17	99XW9	99LC1	99LC2	99LC3	99LC4	99LC5	99LC6	99LC7	99XW1-1	99XW1-2	99XW6	06LC13
Rb	2.27	4.80	4.71	1.79	3.53	1.37	3.67	11.4	33.3	36.0	13.21	63.7	31.7	34.5	48.7	31.9	50.2	42.4	40.6	29.7	36.3	8.97	40.1
Sr	30.32	65.1	65.2	120	178	117	38.8	31.0	115	270	650	2407	445	436	336	406	343	376	376	1584	1631	1883	298
Ba	26.5	49.4	45.5	220	88.9	143	116	97.0	241	643	624	1493	1049	1152	898	1152	780	920	904	1498	2366	922	621
Th	0.06	0.07	0.07	0.07	0.04	0.08	0.03	1.41	0.15	0.73	0.64	0.93	1.80	2.18	2.87	2.49	1.79	3.28	2.93	1.67	1.69	0.70	0.72
U	0.05	0.04	0.03	0.10	0.04	0.17	0.02	0.58	0.08	0.25	0.14	0.25	0.30	0.36	0.31	0.41	0.21	0.46	0.43	1.08	0.69	0.11	0.22
Pb	2.34	2.24	2.40	3.96	3.74	6.87	2.78	2.92	3.49	7.35	6.47	19.5	12.3	13.9	14.1	14.2	15.9	10.8	11.1	11.0	11.51	11.4	12.1
Zr	28.3	39.8	40.8	69.4	26.7	102	24.6	47.2	42.7	178	137	237	278	247	280	289	276	297	285	93.4	69.9	108	273
Hf	0.96	1.40	1.40	2.12	1.02	2.90	0.97	1.50	1.47	5.07	3.41	6.38	6.87	6.22	6.88	7.99	7.25	7.68	7.43	2.77	2.30	3.09	7.85
Nb	1.26	2.63	2.49	3.98	1.66	4.69	1.76	2.37	2.67	5.25	17.7	25.4	22.1	23.8	36.2	23.7	20.9	35.2	34.5	10.4	12.7	14.1	1.69
Ta	0.09	0.16	0.14	0.21	0.09	0.27	0.09	0.18	0.13	0.19	0.80	1.21	1.09	1.23	1.84	1.33	1.10	1.73	1.69	0.50	0.56	0.67	0.10
Sc	33.5	36.5	37.6	34.4	35.4	34.1	37.1	24.0	36.6	45.8	25.3	37.9	26.2	25.7	23.9	24.9	22.8	36.0	33.7	20.4	28.0	15.6	18.6
V	228	263	265	301	247	327	253	179	268	200	213	310	138	145	174	137	121	314	301	173	191	193	122
Cr	2116	1430	1410	254	2639	120	2680	3476	709	18.6	86.4	409	52.1	48.3	35.1	38.9	60.5	117	123	203	202	262	57.5
Co	91.3	76.3	77.8	65.5	89.5	65.0	88.9	94.9	61.4	35.3	36.1	60.2	24.9	25.2	26.5	24.1	23.7	45.0	43.8	25.7	30.3	29.5	20.2
Ni	406	304	310	156	576	135	566	1325	170	9.79	34.2	168	18.7	20.0	16.6	17.4	24.3	25.7	26.9	77.8	81.7	136	15.2
Cu	27.3	11.1	11.1	47.5	48.9	42.3	88.4	19.46	59.0	31.2	33.3	67.1	33.4	35.6	34.0	36.0	34.2	47.6	46.7	23.8	40.6	38.4	21.2
Be	0.33	0.51	0.52	0.82	0.41	0.97	0.43	0.47	0.57	1.46	1.57	2.72	1.91	2.14	2.80	1.92	1.49	4.69	4.65	1.60	1.53	2.07	1.25
Ga	9.42	13.8	13.5	19.4	10.8	20.7	10.5	12.03	15.9	21.8	22.5	46.6	23.2	22.9	24.3	21.3	24.6	18.9	19.1	23.5	23.1	23.2	25.8
Cs	0.02	0.11	0.12	0.03	0.05	0.04	0.04	0.19	0.17	0.66	0.19	0.27	0.33	0.31	0.37	0.27	0.19	0.90	0.95	1.43	0.65	0.08	2.42
Li	10.1	7.24	8.00	6.77	14.2	15.6	12.1	9.90	47.8	14.1	18.5	27.2	11.7	12.9	14.3	10.7	11.2	14.6	14.9	16.9	12.6	14.3	11.9
La	3.41	6.06	6.20	7.98	6.25	9.53	3.44	8.28	6.87	24.7	58.9	79.6	52.3	59.3	101	59.0	61.4	67.2	66.4	66.4	72.1	77.9	56.9
Ce	11.2	18.6	19.1	23.3	20.2	24.5	11.5	16.5	20.5	55.5	133	180	115	134	238	132	137	162	158	155	175	179	115
Pr	1.30	2.46	2.31	3.22	1.74	3.25	1.74	1.97	2.80	7.71	17.1	21.6	13.8	16.5	33.2	16.1	16.3	20.7	20.5	18.7	22.1	21.9	13.9
Nd	5.38	10.1	9.56	14.1	7.04	14.1	7.45	7.76	12.1	33.1	70.4	86.6	57.6	68.0	140	66.5	65.7	89.2	88.6	76.1	91.9	86.2	51.6
Sm	1.54	2.62	2.81	3.85	1.96	4.12	2.44	1.83	3.44	7.74	13.3	16.5	12.1	14.1	29.4	14.7	12.6	18.5	18.05	13.9	17.5	15.0	8.47
Eu	0.34	0.53	0.54	0.90	0.44	0.96	0.40	0.39	0.76	1.76	3.01	3.69	2.61	2.66	2.25	2.81	2.08	2.75	2.70	2.43	2.94	2.34	1.79
Gd	1.62	2.76	2.63	3.99	2.16	4.03	2.12	2.17	3.21	7.18	10.5	11.2	9.22	11.2	20.8	11.4	8.55	13.5	13.3	8.47	10.9	9.06	5.41
Tb	0.32	0.50	0.47	0.70	0.37	0.78	0.40	0.39	0.65	1.22	1.39	1.53	1.40	1.70	2.94	1.64	1.24	1.94	1.87	0.95	1.42	1.05	0.62
Dy	2.14	3.30	3.35	4.65	2.53	4.98	2.60	2.49	4.08	7.55	7.14	7.67	8.12	9.53	16.1	9.79	6.84	10.9	10.1	4.96	6.81	5.03	2.92
Ho	0.41	0.69	0.67	0.95	0.51	1.00	0.55	0.53	0.83	1.62	1.37	1.37	1.62	1.90	2.90	1.98	1.35	2.07	1.93	0.81	1.15	0.84	0.55
Er	1.35	1.97	2.02	2.75	1.56	2.76	1.68	1.45	2.50	4.29	3.57	3.55	4.53	5.34	8.19	5.73	3.95	5.68	5.56	2.18	3.08	2.20	1.45
Tm	0.20	0.29	0.29	0.38	0.23	0.43	0.23	0.22	0.34	0.63	0.49	0.44	0.63	0.74	1.03	0.81	0.55	0.76	0.74	0.26	0.33	0.25	0.21
Yb	1.34	1.81	1.82	2.54	1.35	2.64	1.51	1.34	2.18	4.06	3.00	2.93	4.10	4.77	6.20	5.01	3.95	4.82	4.64	1.54	1.82	1.49	1.42
Lu	0.20	0.29	0.30	0.39	0.23	0.42	0.23	0.20	0.35	0.61	0.45	0.44	0.68	0.76	0.90	0.76	0.62	0.72	0.72	0.22	0.26	0.22	0.22
Y	10.4	16.6	16.4	22.6	12.6	23.8	13.1	13.2	19.8	41.0	34.5	31.8	42.2	48.7	78.7	45.0	33.8	51.6	48.8	19.4	26.4	19.8	15.5
REE	41.2	68.6	68.5	92.4	59.1	97.2	49.4	58.7	80.4	199	358	449	326	379	681	373	356	452	442	371	433	422	276
La/Yb_N	0.63	0.83	0.84	0.78	1.15	0.89	0.56	1.53	0.78	1.51	4.85	6.74	3.16	3.07	4.01	2.91	3.85	3.45	3.54	10.7	9.78	12.9	9.89
Gd/Yb_N	1.00	1.26	1.19	1.30	1.32	1.26	1.16	1.34	1.22	1.46	2.90	3.17	1.86	1.93	2.77	1.88	1.79	2.31	2.37	4.55	4.93	5.02	3.14

Table 4 (*Continued*)

Sample	Group																							
	Xuwujia gabbronorites (low-Mg group)						Xigou gabbro										Liangcheng granitoids							Khondalite
	99LC20	02SX021	06LC01	99LC15	99LC16-1	99LC18	03JN03	06JN03	06JN05	06JN06	99JN2-1	99JN2-2	99JN2-3	99JN2-4	99JN4	99JN5	06LC27	06ZZ01	BSH-6	TG402	HL401	HL402-2	HL403-2	08SX008
Rb	93.6	9.83	72.3	57.9	69.6	66.7	15.0	6.77	43.4	80.0	22.8	6.40	36.6	1.32	17.6	3.00	87.8	127	66.9	129	116	111	78.2	124
Sr	384	1217	366	347	394	401	1738	444	386	365	479	479	417	399	487	409	358	299	222	384	177	249	204	138
Ba	1393	734	825	1007	908	1483	1017	498	141	227	257	111	286	150	190	91.6	1471	2002	889	1122	682	707	738	362
Th	6.71	2.62	0.27	0.14	0.12	0.08	0.92	0.26	1.39	0.40	1.48	0.22	0.51	0.02	4.81	0.03	0.80	1.06	3.56	6.38	10.9	7.17	13.9	0.07
U	0.65	0.21	0.18	0.13	0.17	0.16	0.21	0.12	0.35	0.22	0.35	0.23	0.11	0.02	0.41	0.01	0.25	0.23	0.26	0.75	0.6	0.41	2.4	0.19
Pb	15.4	7.37	9.58	10.2	10.1	10.8	9.4	2.32	7.16	7.66	9.70	6.80	3.91	2.97	10.7	2.90	14.8	18.6	–	–	–	–	–	47.2
Zr	287	255	209	251	254	266	63.0	27.9	31.8	29.1	27.1	11.6	34.1	43.0	18.0	40.8	401	668	280	316	301	250	406	15.2
Hf	8.21	6.54	5.79	6.52	6.32	7.09	1.70	0.94	1.12	1.02	0.92	0.45	1.16	1.41	0.71	1.36	9.33	16.3	8.26	8.11	7.96	6.64	9.91	0.68
Nb	9.59	10.40	10.9	15.0	18.2	12.1	9.12	2.14	3.82	2.03	1.81	0.79	2.23	1.72	1.92	1.91	17.4	5.49	13.4	13.9	16.4	9.24	78.2	0.12
Ta	0.35	0.72	0.53	0.65	0.88	0.51	0.70	0.07	0.17	0.06	0.10	0.03	0.09	0.05	0.08	0.07	0.64	0.18	0.76	0.63	0.81	0.60	0.62	0.18
Sc	13.1	16.6	19.7	18.6	20.7	17.1	0	42.1	36.0	34.3	32.7	45.6	36.9	35.3	43.7	35.0	15.4	18.1	20.3	13.6	15.9	17.7	13.5	0.19
V	108	151	141	122	150	101	0	145	134	138	129	451	154	150	494	152	124	54.5	88.6	113	85.5	79.6	80.6	0.67
Cr	134	28.4	71.4	85.9	233	132	48.7	16.7	50.7	49.1	192	106	276	210	36.8	206	27.9	3.39	94.9	85.2	61.4	55.5	79.6	0.90
Co	16.6	23.7	23.6	23.9	27.5	22.3	25.3	47.0	38.7	38.2	39.1	68.3	45.9	46.2	64.1	48.9	15.6	9.21	23.1	14.0	13.8	11.8	10.6	0.09
Ni	50.9	8.50	21.9	19.1	92.7	48.0	22.0	31.7	60.3	59.2	104	71.4	145	110	34.1	109	8.48	0.17	18.0	14.6	17.5	14.3	11.4	0
Cu	13.8	25.5	18.9	22.4	27.1	21.9	27.7	37.0	39.0	55.5	30.4	22.9	37.6	44.3	19.2	94.1	19.6	7.17	–	–	–	–	–	6.80
Be	0.99	1.62	2.01	1.23	1.65	1.01	0	0.43	1.09	1.03	0.28	0.39	0.40	0.38	0.47	0.40	1.27	1.35	–	–	–	–	–	0.29
Ga	21.0	19.7	24.3	22.6	24.5	21.1	22.3	16.0	16.5	16.3	15.3	15.6	15.1	15.7	16.0	15.7	21.5	23.7	–	–	–	–	–	12.1
Cs	2.44	0.07	0.44	0.07	0.09	0.05	0.44	0.22	0.36	0.60	0.28	0.26	0.30	0.22	0.40	0.32	1.16	0.75	2.27	0.88	1.55	0.67	0.20	0.25
Li	14.9	32.4	19.0	15.3	16.6	14.2	0	9.07	21.4	15.0	9.20	4.82	14.9	8.89	7.15	5.31	18.4	4.12	–	–	–	–	–	12.1
La	94.0	63.8	28.5	37.7	30.6	35.7	64.9	6.48	9.03	9.84	11.9	3.52	6.63	7.00	6.98	6.60	51.7	71.7	53.3	46.2	72.7	51.5	48.6	12.2
Ce	189	122	61.8	82.9	71.9	77.4	142	15.3	22.1	21.6	16.9	7.22	18.3	19.0	13.2	18.1	107	153	113	79.2	159	97.6	81.1	18.6
Pr	24.0	15.6	8.04	9.90	8.76	8.96	17.4	2.02	3.00	2.80	2.23	0.99	2.33	2.48	1.56	2.24	13.4	19.5	13.9	8.78	18.3	11.7	8.66	1.84
Nd	95.4	60.3	31.9	40.2	37.7	38.0	67.5	8.50	12.8	11.0	8.30	3.76	9.84	10.5	6.08	9.85	50.9	77.3	54.1	32.1	69.8	47.0	31.7	5.72
Sm	15.9	9.33	6.46	7.81	7.93	7.36	10.9	1.86	2.86	2.24	1.87	1.01	2.41	2.57	1.39	2.52	9.18	14.5	10.9	5.60	12.4	9.6	5.36	0.66
Eu	1.94	2.33	1.90	1.98	1.89	2.06	2.15	0.73	0.74	0.72	0.57	0.40	0.70	0.66	0.48	0.72	2.36	2.98	1.65	0.94	1.49	1.27	1.06	1.08
Gd	9.44	6.56	4.80	5.41	6.07	5.16	7.99	1.74	2.59	2.01	1.61	1.02	1.99	2.10	1.39	2.13	6.91	12.5	9.41	4.00	8.45	6.71	4.26	0.31
Tb	1.13	0.85	0.66	0.67	0.81	0.69	1.08	0.28	0.41	0.31	0.26	0.18	0.33	0.33	0.21	0.36	0.86	1.77	1.40	0.67	1.23	1.04	0.73	0.03
Dy	5.81	4.09	3.09	3.72	4.38	3.33	4.55	1.63	2.31	1.75	1.63	1.17	1.95	2.14	1.33	2.16	4.15	9.87	8.36	3.89	5.89	6.11	4.35	0.10
Ho	0.97	0.75	0.56	0.63	0.74	0.60	0.73	0.34	0.45	0.35	0.31	0.22	0.42	0.38	0.28	0.44	0.78	1.88	1.67	0.78	1.08	1.17	0.86	0.02
Er	2.20	2.05	1.42	1.81	1.98	1.53	1.90	0.88	1.19	0.96	0.87	0.67	1.17	1.14	0.80	1.24	2.02	4.94	5.41	2.42	3.08	3.32	2.67	0.06
Tm	0.26	0.30	0.20	0.24	0.25	0.20	0.23	0.14	0.18	0.15	0.13	0.10	0.17	0.16	0.12	0.18	0.29	0.67	0.73	0.36	0.40	0.44	0.38	0.01
Yb	1.53	1.90	1.27	1.39	1.51	1.34	1.34	0.93	1.20	0.99	0.85	0.59	1.07	1.04	0.73	1.20	1.93	4.20	4.79	2.42	2.64	2.89	2.71	0.09
Lu	0.22	0.28	0.19	0.22	0.25	0.22	0.20	0.13	0.16	0.15	0.14	0.09	0.17	0.16	0.11	0.18	0.29	0.63	0.72	0.38	0.38	0.41	0.41	0.02
Y	23.6	18.7	16.4	15.2	20.3	14.0	18.7	9.34	12.6	9.98	7.39	5.31	9.63	9.64	6.22	10.1	20.7	46.7	46.5	22.7	28.4	32.9	24.8	0.32
REE	465	308	167	209	195	196	341	50.3	71.6	64.9	55.0	26.3	57.1	59.1	40.9	58.0	273	422	326	210	385	274	218	41.1
La/Yb_N	15.2	8.31	5.54	6.72	5.00	6.58	12.0	1.73	1.87	2.46	3.45	1.48	1.53	1.67	2.37	1.36	6.62	4.22	2.75	4.72	6.81	4.41	4.44	33.5
Gd/Yb_N	5.11	2.86	3.12	3.22	3.32	3.18	4.93	1.55	1.79	1.68	1.57	1.44	1.53	1.67	1.58	1.47	2.96	2.46	1.63	1.37	2.65	1.92	1.30	2.85

Notes: La/Yb_N and Gd/Yb_N values are La/Yb and Gd/Yb ratios normalized to chondrite values after Sun and McDonough (1989). Entries with "–" refer to data undetermined. Data of samples BSH-6, TG402, HL401, HL402-2 and HL403-2 are from Zhong et al. (2006).

Table 5
Selected whole-rock Nd isotopic data of the Xuwujia gabbronorites and associated rocks.

Sample	Group																	
	Xuwujia gabbronorites (high-Mg group)											Xuwujia gabbronorites (low-Mg group)						
	99XBY-4	99XBY5-1	99XBY5-2	99XBY6-1	99XBY6-2	99XBY6-4	99XBY-8	99XW-3	99XW-7	99XW15	99XW16	06LC07	06LC17	99XW9	99LC1	99LC2	99LC3	99LC4
Sm (ppm)	1.261	2.282	2.272	3.472	1.652	3.787	1.807	2.858	2.843	1.931	1.665	7.554	12.221	16.91	11.05	12.73	26.83	12.15
Nd (ppm)	4.948	9.367	9.357	13.48	6.567	14.61	7.101	11.67	17.08	9.248	7.098	32.10	66.011	98.78	57.37	65.49	138.9	62.75
$^{147}Sm/^{144}Nd$	0.1541	0.1474	0.1468	0.1558	0.1521	0.1567	0.1539	0.1482	0.1007	0.1263	0.141	0.1423	0.1119	0.1035	0.1165	0.1176	0.1168	0.1171
$^{143}Nd/^{144}Nd$	0.512194	0.512066	0.512107	0.512155	0.512089	0.512183	0.512217	0.512003	0.511313	0.51184	0.512053	0.51192	0.511487	0.511288	0.511545	0.511589	0.511564	0.511588
error, 2σ	0.000011	0.000009	0.000008	0.000008	0.000008	0.000009	0.000007	0.00001	0.000009	0.000009	0.000009	0.000011	0.00001	0.000009	0.000007	0.000006	0.000007	0.000007
T_{DM}, Ma	2433	2480	2365	2605	2611	2572	2367	2654	2466	2275	2291	2610	2478	2562	2504	2464	2482	2453
εNd_0	−8.6	−11.1	−10.3	−9.4	−10.7	−8.8	−8.2	−12.4	−25.8	−15.5	−11.4	−14.0	−22.5	−26.3	−21.3	−20.4	−20.9	−20.4

Sample	Group																	
	Xuwujia gabbronorites (low-Mg group)																	
	99LC5	99LC6	99LC7	99XW1-1	99XW1-2	99XW6	02SX021	99LC15	99LC16-1	99LC18	99LC20	99LC21	99XW4-1	99XW4-2	99XW5	99XW5-1	99XW5-2	99XW5-3
Sm (ppm)	11.67	16.46	16.2	10.88	14.12	12.16	10.375	6.339	8.902	7.446	9.187	4.317	18.678	16.892	3.167	6.964	2.68	2.653
Nd (ppm)	64.66	86.15	85.2	68.11	81.77	75.75	66.069	37.33	46.36	49.89	44.24	22.58	113.725	103.486	13.11	42.49	11.4	11.13
$^{147}Sm/^{144}Nd$	0.1092	0.1155	0.115	0.09661	0.1044	0.09712	0.0951	0.1027	0.1161	0.0903	0.1256	0.1157	0.09933	0.09872	0.1462	0.09914	0.1422	0.1441
$^{143}Nd/^{144}Nd$	0.511457	0.511527	0.511506	0.511279	0.511333	0.51124	0.511093	0.511379	0.511555	0.511279	0.511646	0.511518	0.511313	0.511325	0.511995	0.511287	0.511884	0.512043
error, 2σ	0.000007	0.000008	0.000007	0.000009	0.000008	0.000008	0.000014	0.000007	0.000009	0.000006	0.000009	0.000009	0.000009	0.000009	0.000008	0.000017	0.000007	0.00001
T_{DM}, Ma	2457	2506	2526	2424	2521	2485	2628	2420	2479	2300	2588	2525	2436	2408	2594	2467	2684	2413
εNd_0	−23.0	−21.6	−22.04	−26.5	−25.4	−27.2	−30.1	−24.5	−21.1	−26.5	−19.3	−21.8	−25.8	−25.6	−12.5	−26.3	−14.7	−11.6
εNd_t	−1.4	−1.6	−1.9	−1.7	−2.6	−2.6	−5.0	−1.3	−1.2	−0.2	−1.7	−1.8	−1.7	−1.3	−0	−2.2	−1.2	1.4

Sample	Group																
	Xuwujia gabbronorites (low-Mg group)				Liangcheng granitoids	Xigou gabbro											Khondalite
	99XW100	99XW101	99LC17	99XW1	06LC27	06JN03	06JN05	06JN06	99JN2-1	99JN2-2	99JN2-3	99JN2-4	99JN4	99JN5	99JN2-5	99JN3	HT2-9
Sm (ppm)	8.76	5.721	6.098	18.43	8.658	1.694	2.057	2.632	1.668	0.867	1.758	1.951	1.556	1.842	1.949	1.251	5.70
Nd (ppm)	49.72	36.384	34.12	111.786	49.997	7.472	9.757	11.161	8.184	3.565	8.263	9.34	7.512	8.371	9.092	5.941	27.50
$^{147}Sm/^{144}Nd$	0.1066	0.0951	0.1081	0.09971	0.1047	0.137	0.1275	0.1425	0.1233	0.1471	0.1287	0.1263	0.1261	0.1331	0.1296	0.1274	0.1251
$^{143}Nd/^{144}Nd$	0.511435	0.511328	0.511423	0.511329	0.511428	0.511703	0.511628	0.511741	0.511448	0.511723	0.511555	0.511488	0.511535	0.511574	0.51151	0.511563	0.511495
error, 2σ	0.000007	0.000007	0.000007	0.000008	0.000011	0.000018	0.000009	0.000011	0.000009	0.000009	0.000012	0.000007	0.000011	0.000009	0.000008	0.000017	0.000007
T_{DM}, Ma	2429	2331	2480	2423	2396	2859	2674	2998	2852	3242	2843	2880	2793	2961	2953	2786	2830
εNd_0	−23.4	−25.5	−23.7	−25.5	−23.6	−18.2	−19.7	−17.5	−23.2	−17.8	−21.1	−22.4	−21.5	−20.7	−22.0	−20.9	−22.3
εNd_t	−1.2	−0.4	−1.8	−1.5	−0.8	−3.5	−2.6	−4.1	−5.1	−5.6	−4.3	−5.0	−4.0	−5.0	−5.4	−3.8	−4.6

Notes: T_{DM} ages are calculated after DePaolo (1981).εNd_0 is the present day value, and εNd_t values are calculated back to 1930 Ma. Khondalite data (HT2-9) are after Wan et al. (2000).

Isoplot 3.0 programs (Ludwig, 2002, 2003). The data in Table 1 are given with 1σ errors. Analytical procedures of CAMECA and SHRIMP ion probes were similar to those described in Li et al. (2009) and Williams (1998), respectively.

Zircon *in situ* Hf isotope analyses (Table 2) were determined using a Neptune MC-ICPMS. A 63-μm spot size was applied during ablation with a 193 nm laser, using a repetition rate of 10 Hz in most cases. During analysis, isobaric interference corrections of ^{176}Lu on ^{176}Hf were not processed due to the extremely low ^{176}Lu/^{177}Hf in zircon (normally <0.002), although ^{175}Lu/^{176}Lu = 0.02655 is used for elemental fractionation correction. The isobaric interference of ^{176}Yb on ^{176}Hf was corrected using the mean fractionation index proposed by Iizuka and Hirata (2005). A value of 0.5886 was used for the ^{176}Yb/^{172}Yb ratio (Chu et al., 2002; Vervoort et al., 2004). The data reported here were corrected assuming a ^{176}Hf/^{177}Hf ratio of 0.282305 for zircon 91500 (after Wu et al., 2006).

Major element determinations were performed by X-ray fluorescence (Shimadzu XRF-1700/1500) after fusion with lithium tetraborate. The analyses were corrected using Chinese national standard sample GBW07101-07114. The precision was better than 0.2 wt.% in the analysis range. The loss-on-ignition was measured as the weight loss of the samples after 1 h baking under a constant temperature at 1000 °C. Trace element analyses were determined using an ELEMENT ICP-MS after HNO_3 + HF digestion of about 40 mg sample powder in a Teflon vessel, with accuracy and reproducibility monitored using Chinese national standard samples GSR1 (granite), GSR2 (rhyolite) and GSR3 (basalt). The relative standard deviation was better than 5% above the detection limits. Nd isotope determinations were performed on a Finnigan MAT 262 spectrometer; Nd was measured as a metal. The data were normalized to ^{146}Nd/^{144}Nd = 0.7219 to correct for instrumental fractionation. The Ames Nd standard reference material was used to quantify analytical bias; however, no adjustment was applied to the unknowns as the measurements for the standard agree with the standard value, within error, during this analytical session (^{143}Nd/^{144}Nd = 0.512138 ± 17, 2σ, n = 18, data of October, 2006). Procedural blank for Sm–Nd isotope analyses were better than 50 pg. The external precision (2σ) of ^{147}Sm/^{144}Nd ratios was better than 0.5%.

5. Geochronology

5.1. Samples 06LC17 (Hongmiaozi gabbronorite dyke) and 02SX021 (Xuwujia norite dyke)

This gabbronoritic dyke (part of the low-Mg group of Xuwujia gabbronorites, see Section 6) intruded the khondalite but is itself intruded by granitoids near Hongmiaozi village (GPS: N40°35′, E112°21′; Fig. 1). Zircon grains separated from this sample (06LC17) have lengths of 200 μm or larger. They have irregular shapes with distinct large, dark cores and thin, light-coloured rims (Fig. 3a). The rim domains have distinctly lower Th and U contents (mostly <100 ppm) and Th/U ratios (mostly 0.2–0.5) than the core domains (mostly >100 ppm and Th/U between 0.6 and 0.9, respectively) (Fig. 4a).

U–Th–Pb analyses were initially acquired using the SHRIMP ion probe. For the core domains of zircon grains, the ^{207}Pb/^{206}Pb ages ranges from 2047 ± 21 to 1873 ± 23 Ma, with an average age of 1964 ± 9 [2σ] Ma (MSWD = 4.4, n = 19; Table 1A and Fig. 5a). For the rim domains, the ages from different spots are not consistent: eight analyses yield a weighted mean ^{207}Pb/^{206}Pb age of 1907 ± 37 [2σ] Ma (MSWD = 3.6, n = 9; Table 1A and Fig. 5a). The relatively large analytical spot size (30–40 μm) employed during these analytical sessions leaves open the possibility that some of the analytical scatter is due to inadvertent overlapping of core and rim domains, yielding mixed and geologically meaningless age information. Therefore, the smaller diameter primary ion beam capability of the CAMECA ion probe (~20 μm) was employed on these same zircons. Twenty-seven analyses from core domains yield a weighted mean ^{207}Pb/^{206}Pb age of 1954 ± 6 [2σ] Ma (2σ, MSWD = 2.3, n = 27; Table 1B and Fig. 5b); in contrast, 13 analyses from the rims yield a weighted mean ^{207}Pb/^{206}Pb age of 1925 ± 8 [2σ] Ma (2σ, MSWD = 0.38, n = 13; Fig. 5b). There are several possibilities for the explanation of these ages, i.e. (1) 1925 Ma is the age of a metamorphic event and 1954 Ma is close to the crystallization age or an average of inherited ages or a mixture of both; (2) 1925 Ma represents the crystallization age and the 1954 Ma is an average of inherited ages. In any case, this dyke is likely intruded at an age no younger than 1.925 Ga and no older than 1.954 Ga.

Other ages have been reported from the Xuwujia dyke (GPS: N40°44′, E113°15′). Guo et al. (2001) reported a weighted mean ^{207}Pb/^{206}Pb age at 1921 ± 1 Ma using TIMS methods and interpreted this as the magmatic age. But zircon grains from this dyke are round and multifaceted, and likely have rim and core domains (Fig. 3b). Peng et al. (2005) analyzed different domains of the zircon grains using a SHRIMP ion probe, but they were averaged together and gave a weighted mean ^{207}Pb/^{206}Pb age of 1929 ± 8 Ma, which was interpreted as a metamorphic age (sample 02SX021, quartz monzonorite, low-Mg group of Xuwujia gabbronorites, see Section 6). Here we recalculated these data using only core domains, yielding a weighted mean ^{207}Pb/^{206}Pb age of 1931 ± 8 [2σ] Ma (MSWD = 0.71, n = 14) (Fig. 5c). As these spots have very high Th/U ratios, mostly around 2.0, which are more consistent with a magmatic signature (e.g., Hoskin and Schaltegger, 2003), it is interpreted as the crystallization age of the dyke. In addition, two spot analyses from rim domains are slightly younger (1862 ± 19 [1σ] and 1891 ± 18 [1σ] Ma), and could represent ages of overgrowth during metamorphism and/or late neighboring intrusion of the Liangcheng granitoids.

The Lu–Hf isotopes of different zircon domains were analyzed (Table 2). These data show different εHf_t (t = 1.93 Ga) values between rim and core domains of sample 06LC17, although there are big variations in the cores (Fig. 4b). The core domains have lower εHf_t values that are more likely to be inherited from precursor rocks, whereas the rim domains have higher εHf_t values, similar to that of cores of the sample 02SX021, and are possibly due to overgrowth from juvenile magma. Thus we would interpret the ca. 1.93 Ga ages (1925 Ma of 06LC17 and 1931 Ma of 02SX021) to be related to magmatism, although the possibility of a crystallization age of ≤1.954 Ga but ≥1.925 Ga for Hongmiaozi dyke (06LC17) remains open. These ca. 1.93 Ga ages are quite close to the high-temperature metamorphic ages in the accompanying metasediments (e.g., Santosh et al., 2006, 2007b; Liu et al., 2009a,b).

5.2. Sample 06JN05 (Xigou gabbro)

Sample 06JN05 is from the gabbro near the village of Xigou (GPS: N41°01′, E112°59′; Fig. 1b). Zircon grains from this sample are slightly elongate and subhedral showing cracked rims surrounding homogeneous center domains (Fig. 3b). They have high Th and U contents up to 3057 and 7407 ppm, respectively (Table 1A and Fig. 4a), and the cracks could be caused by radioactive damage due to Th and U, or alternatively by differential expansion of cores and rims during decompression. The Th/U ratios vary from 0.07 to 0.51, but are mostly around 0.1 (Fig. 4a). The discordance of each spot is positively correlated with U content (Fig. 5d inset). Similar high U bias by SHRIMP analysis is reported by Williams and Hergt (2000) and it is thought to have no effect on the measurement of ^{207}Pb/^{206}Pb ages. Fourteen analyses from cores give a weighted mean ^{207}Pb/^{206}Pb age of 1857 ± 4 [2σ] Ma (MSWD = 2.0, n = 14; Table 1A and Fig. 5d). Two analyses from rim domains (spots

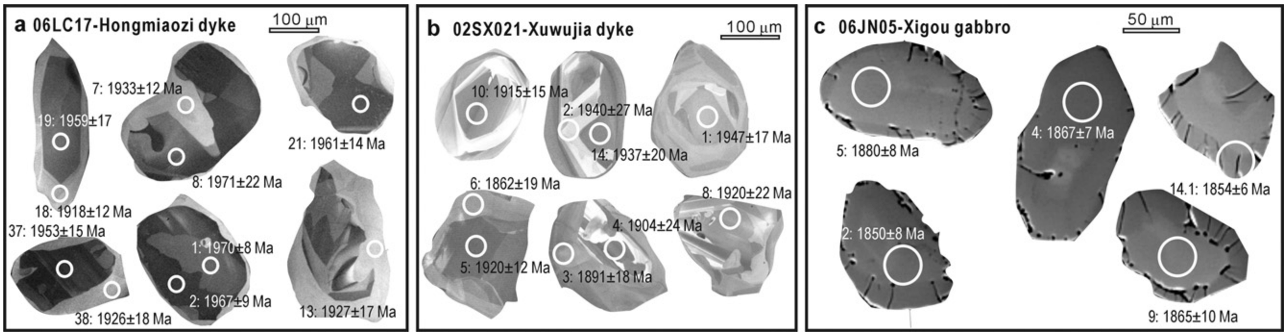

Fig. 3. Representative cathodoluminescence (CL) and backscattered electron (BSE) images of selected zircons. (a) 06LC17 (CL, Hongmiaozi dyke): zircon grains have sizes of 200 μm or larger, and irregular shapes with distinct large, dark cores and thin, bright rims. (b) 02SX021 (CL, Xuwujia dyke): zircons are round and multifaceted. (c) 06JN05 (BSE, Xigou gabbro): zircons are slightly elongate and subhedral showing cracked rims surrounding homogeneous cores. The labeled age results are analyses by CAMECA ion probe for 06LC17 and SHRIMP ion probe for 02SX021 and 06JN05.

13.1 and 14.1) give $^{207}Pb/^{206}Pb$ ages at 1857 ± 5 [1σ] and 1881 ± 8 [1σ] Ma, no younger than those from grain-center domains. As the rock has experienced metamorphism, this age could represent a metamorphic event. This agrees with the observation that the Xigou gabbro was intruded by the ca. 1.93–1.89 Ga Liangcheng granitoids, and thus should have an age no younger than ca. 1.90 Ga. Moreover, these rim ages may instead reflect isotopic disturbance rather than robust metamorphic overgrowth ages because these domains are distinguished by numerous cracks; further analysis is required to determine if the timing of centre and rim domain growth is statistically distinct.

6. Geochemistry

6.1. Alteration, metamorphism and significance of whole-rock compositions

Low grade and/or fluid-assisted alteration processes have the potential to modify whole-rock chemistry selectively, manifest most obviously by high loss-on-ignition (LOI) values, as well as some scattering (through variable mobility) of major elements, and addition or subtraction of the large-ion lithophile elements (LILE) (e.g., Rb, Sr, and Ba) (Chesworth et al., 1981; Wood et al., 1979; Pandarinath et al., 2008). High-grade metamorphism may also result in significant element mobility. In contrast, high field-strength elements (HFSE) and rare earth elements (REE) are relatively immobile during metamorphism, and in general tend to reflect igneous processes (Wood et al., 1979; Middelburg et al., 1988). Analyses of samples from the study area exhibit low LOI values (mostly <2 wt.%). And although LILE mobilization is evident in some samples, most major elements, REEs and HFSEs exhibit coherent variations among geological bodies and groups (Figs. 6–8), and thus likely reflect original characteristics. We carefully selected such relatively immobile elements for our interpretations; for instance, we utilized immobile trace elements in variation diagrams (Fig. 7) and spidergrams (Fig. 8b).

It is important to mention here that different groups of the gabbronorites, irrespective of whether samples were collected from fine- or coarse-grained portions, show parallel trace element patterns (Fig. 8). As samples from fine-grained chilled margins could represent parental compositions (see Latypov et al., 2007), and because they have parallel trace element patterns with those from other portions, we suggest that the whole-rock compositions of most samples are close to the compositions of the liquid from which these rocks crystallized.

6.2. The Xuwujia gabbronorites

The Xuwujia gabbronorites are composed mainly of gabbronorite, but also include some norite, olivine gabbronorite, monzonorite, quartz gabbronorite, and quartz monzonorite. They can be divided into two groups according to their MgO contents and Mg# (Mg numbers, calculated as molar 100 × $Mg/(Mg + Fe^{2+})$): a high-Mg gabbronoritic group (high-Mg group) with MgO content of 6.2–22.9 wt.% and Mg# of 51–82, and a relatively low-Mg gabbronoritic group with MgO content of 2.2–5.7 wt.% and Mg# of 35–57 (Table 3). They are distinct in most chemical diagrams (e.g., Figs. 6–8). The high-Mg group is mostly seen as dykes and sills in the khondalite, whereas the low-Mg group occurs more widely, in the khondalite and adjacent rocks, as well as in the granitoids.

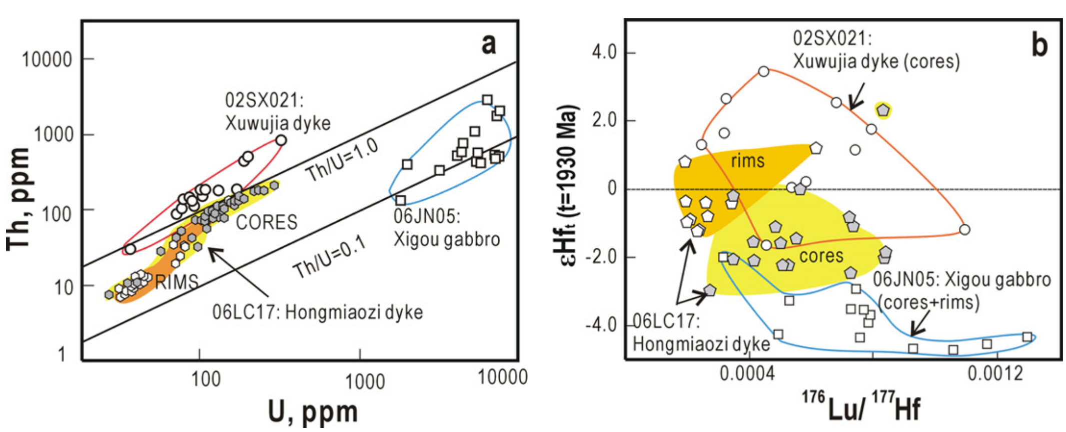

Fig. 4. Zircon trace element and Hf isotopic results: (a) Th versus U plot; (b) εHf_t (t = 1930 Ma) versus $^{176}Lu/^{177}Hf$ diagram.

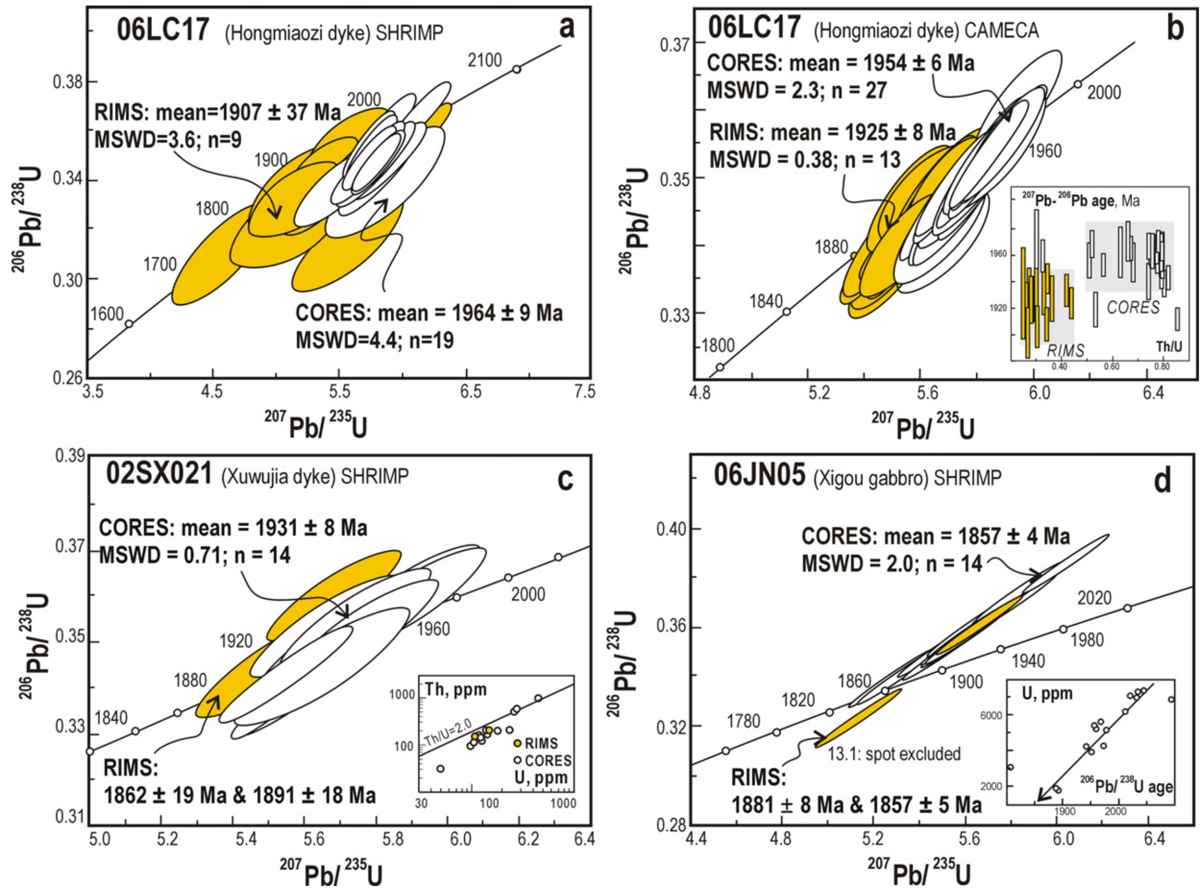

Fig. 5. U–Pb zircon concordia diagrams for samples 06LC17 (Hongmiaozi dyke) and 06JN05 (Xigou gabbro). (a) SHRIMP data for 06LC17; (b) CAMECA data for 06LC17, inset: $^{207}Pb/^{206}Pb$ age versus Th/U plot; (c) SHRIMP data for 02SX021 (inset: Th versus U plot for the analyzed spots; shaded circles represent rim compositions); and (d) SHRIMP data for 06JN05, inset: U versus $^{206}Pb/^{238}U$ age plot. "Mean" refers to average $^{207}Pb/^{206}Pb$ ages.

The high-Mg rocks are composed of olivine, orthopyroxene (hypersthene), clinopyroxene, hornblende, and plagioclase. They show variable SiO_2 (45.4–50.6 wt.%), Al_2O_3 (6.61–17.95 wt.%), CaO (6.03–16.90 wt.%) and Fe_2O_3t (total iron, 8.9–13.6 wt.%) contents. They have low TiO_2 (0.39–1.02 wt.%), Na_2O (0.44–1.21 wt.%), K_2O (0.10–1.37 wt.%), and P_2O_5-contents (<0.23 wt.%) (Table 3). The high-Mg rocks are chemically similar to komatiite or high-Mg tholeiite. Normalized to chondrite values of Sun and McDonough (1989), they generally have flat REE patterns with slight light rare earth element (REE) enrichment (La/Yb_N = 0.56–1.53; Table 4) (Fig. 8a) and negative Eu-anomalies (Eu/Eu^* = 0.53–0.72, $Eu/Eu^* = Eu_N/[(Sm_N)^*(Gd_N)]^{-1/2}$). Accompanying multi-element spidergrams, normalized to primitive mantle of Sun and McDonough (1989), also show slightly negative anomalies in HFSE (e.g., Th, Nb, Zr, and Ti) compared with the neighboring elements (Fig. 8b). Their εNd_t (t = 1.93 Ga) values vary from +0.3 to +2.4 (one outlier at −2.1), mostly between +1.0 and +2.0 (Table 5).

The low-Mg rocks are composed of hypersthene, clinopyroxene, hornblende, and plagioclase, with or without quartz and/or garnet. This group has large variation in SiO_2 contents, varying from 48.9 to 59.7 wt.%. It is also characterized by variable Al_2O_3 (14.88–19.28 wt.%), CaO (4.90–8.67 wt.%), Fe_2O_3t (6.8–15.8 wt.%), K_2O (0.68–3.23 wt.%) and P_2O_5 (0.21–1.23 wt.%) contents, but high TiO_2 (0.98–3.20 wt.%), and Na_2O (1.83–3.21 wt.%) contents (Table 3).The low-Mg samples mostly plot in the tholeiitic field, with a few in the calc-alkaline field (Fig. 6b). In the covariant plots

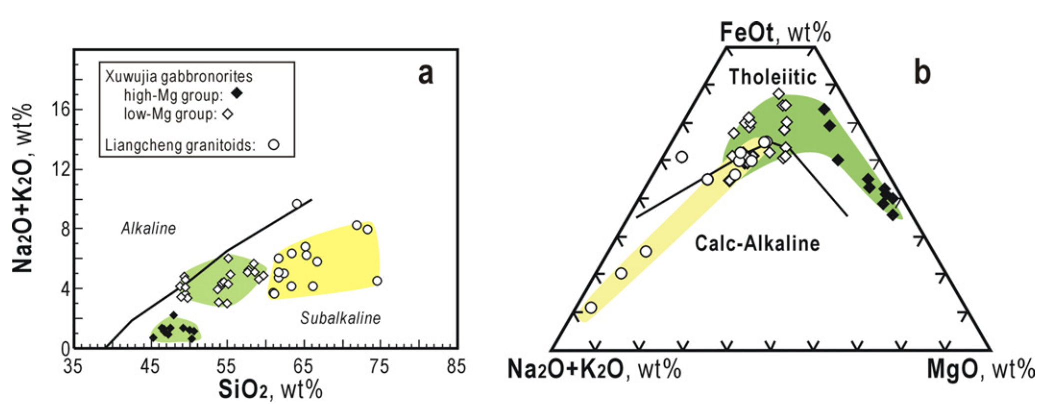

Fig. 6. (a) $Na_2O + K_2O$ versus SiO_2 diagram, and (b) FeOt–$Na_2O + K_2O$–MgO diagram (after Irvine and Baragar, 1971).

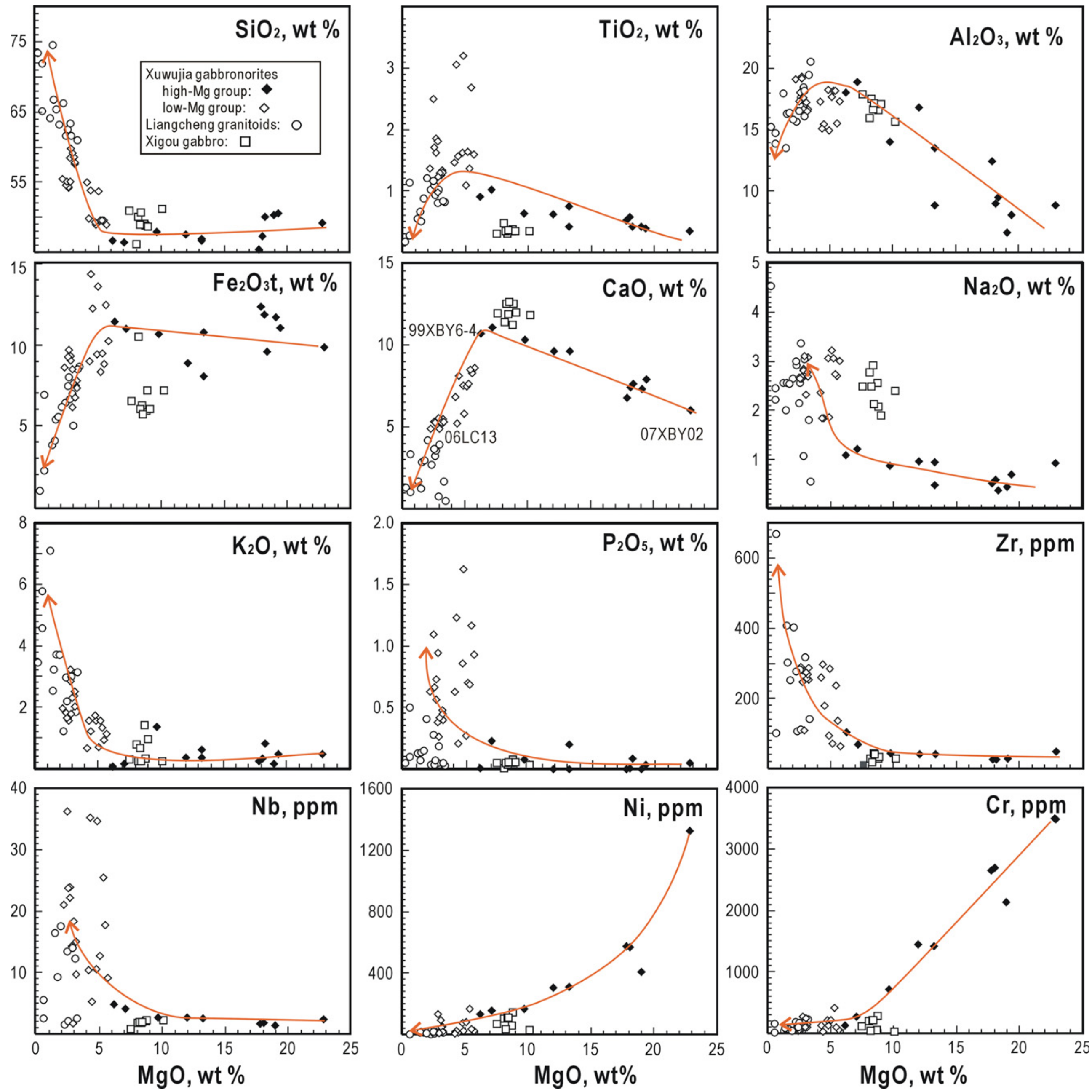

Fig. 7. Variation diagrams of selected major oxides and trace elements versus MgO (wt.%). The red curves portray the possibly differentiation trend of the liquid of the gabbronorites.

between MgO and other major/trace elements, some elements are well correlated (e.g., SiO_2, CaO, and K_2O; Fig. 7), whereas some others show considerable scatter (e.g., TiO_2, Fe_2O_3t, P_2O_5, and Nb; Fig. 7). They have negative Eu-anomalies (Eu/Eu* = 0.48–1.05) and distinct light REE enriched patterns (La/Yb_N = 1.51–12.0, with one at 15.2) (Fig. 8a). The majority shows variable negative anomalies in HFSEs (e.g., Th, Nb, Zr, and Ti) (Fig. 8b). Their εNd_t (t = 1.93 Ga) values vary from −5.0 to 0 (Table 5).

6.3. The Liangcheng granitoids

The Liangcheng granitoids comprise garnet-bearing granite, granodiorite and quartz-rich granitic compositions. They have SiO_2 contents of 65.0–74.5 wt.%, MgO contents of 0.3–3.4 wt.% (Mg# of 37–54, with one exception at 16), Al_2O_3 contents of 13.45–20.50 wt.%, Fe_2O_3t contents of 1.2–8.9 wt.%, CaO contents of 0.40–4.19 wt.%, TiO_2 contents of 0.98–3.20 wt.%, K_2O contents of 0.28–2.21 wt.%, Na_2O contents of 0.54–4.51 wt.% (mostly around 2.50 wt.%), and P_2O_5-contents of less than 0.50 wt.% (data of Zhong et al., 2006, Lan, 2006 and this study; Fig. 7 and Table 3). They are calc-alkaline (Fig. 6b) and peraluminous, and were identified as S-type granites by previous workers (e.g., Zhai et al., 2003; Zhong et al., 2006; Lan, 2006). Most major oxides and some minor and trace elements show continuous variations (Fig. 7). They are enriched in light REEs (La/Yb_N = 1.18–6.81) with negative to positive Eu-anomalies (Eu/Eu* = 0.14–1.23) (Fig. 8a). They show large variations in behaviour in the HFSEs, for instance, negative anomalies for Nb and Ti, variable Th anomalies, and slight positive anomalies for Zr (Fig. 8b). The single sample analyzed for Sm–Nd isotopes has an initial εNd (1.93 Ga) value of −0.8 (Table 5). They have trace element patterns similar to the low-Mg group of gabbronorites (Fig. 8a and b).

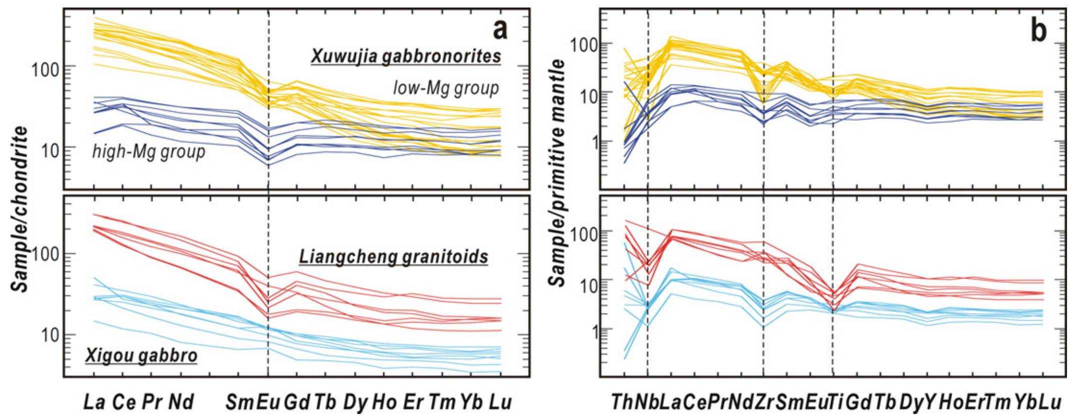

Fig. 8. Chondrite-normalized REE patterns (a) and primitive mantle-normalized trace element spidergrams (b). Chondrite and primitive mantle-normalized values are from Sun and McDonough (1989).

6.4. The Xigou gabbro

The rocks of the Xigou gabbro have high Mg# (56–72) (Table 3). They have high MgO (7.5–10.1 wt.%), Al_2O_3 (13.45–20.50 wt.%), CaO (11.25–12.62 wt.%, and Na_2O (2.11–2.90 wt.%) contents, low SiO_2 (46.2–51.1 wt.%), TiO_2 (0.31–0.48 wt.%), K_2O (0.25–1.44 wt.%), and P_2O_5 (~0.05 wt.%) contents, and varied Fe_2O_3t contents (6.3–11.6 wt.%) (Fig. 7 and Table 3). On the covariant element plots (Fig. 7) they show a restricted range. They have moderately enriched light REEs (La/Yb_N = 1.48–3.45) with small Eu-anomalies (Eu/Eu^* = 0.83–1.23) (Fig. 8a). They show negative anomalies for most HFSEs (e.g., Nb, Zr, and Ti), with variable anomalies in Th-content (Fig. 8b). Their εNd_t (t = 1.93 Ga) values vary from −5.6 to −2.6 (Table 5).

7. Discussions

7.1. The Liangcheng granitoids and the Xigou gabbro: melts and cumulate

The weight of field and petrological studies suggest that the Liangcheng granitoids are mostly derived from metasediments (the khondalite, e.g., Zhai et al., 2003; Lan, 2006; Zhong et al., 2006, 2007). These granitoids range up to relatively high Mg numbers (up to 54), and show some chemical affinities with the low-Mg gabbronorites (Fig. 8a and b). This could have resulted from local mixing with gabbronoritic melts. The Xigou gabbro contains magnetite-layers, as well as gabbroic parts (clinopyroxene and plagioclase). It can be considered as a cumulate. The narrow com-

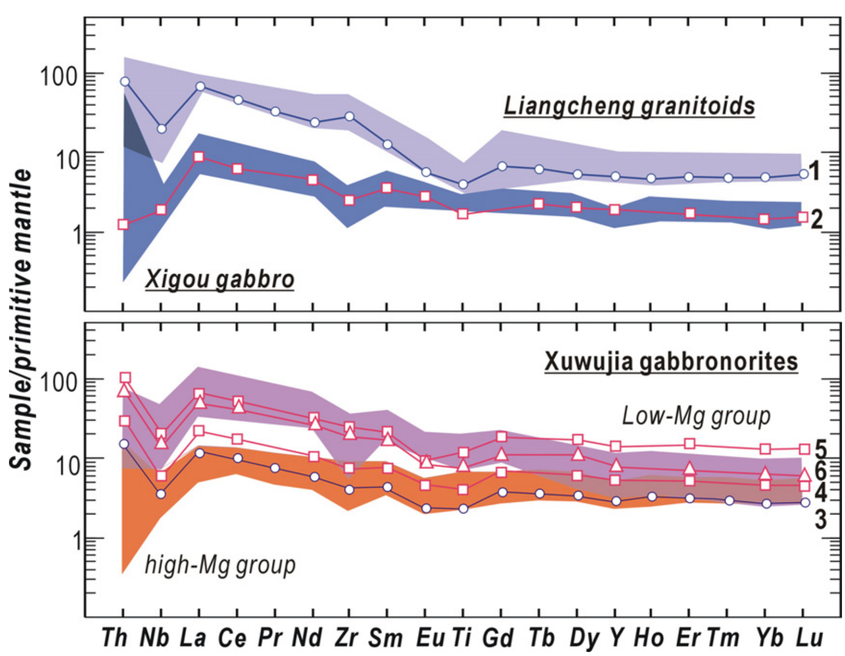

Fig. 9. Model calculation for the Liangcheng granitoids, the Xigou gabbro and the Xuwujia gabbronorites. Curve 1 shows the pattern of sample TG402 (Liangcheng granitoid); curve 2 is the composition of a solid assemblage composed of 0.05 (mol proportion) magnetite, 0.35 clinopyroxene, and 0.60 plagioclase (an assemblage similar to those in the Xigou gabbro, Table 3), which is in equilibrium with a magma composition represented by curve 1; curve 3 is the pattern of sample 07XBY02 (high-Mg group); curve 4 presents a composition after fractional crystallization of 45 vol.% portion of melt from a liquid represented by curve 3 with fractional components including 62 mol% olivine and 38 mol% hypersthene; and curve 5 refers to a composition after 71 vol.% portion of fractional crystallization of 17 mol% olivine, 22 mol% clinopyroxene and 61 mol% plagioclase from a liquid represented by curve 4. Curve 6 is a mix composition of 70 vol.% of curve 5 and 30 vol.% of khondalite melt represented by sample 02SX008 (Tables 3, 4). Partition coefficients for granitoids are from Luhr and Carmichael (1980) (REE and Th of clinopyroxene and plagioclase), Beattie (1993b) (REE and Th of magnetite), Larsen (1979)(Y, Zr and Nb of clinopyroxene), Dunn and Sen (1994) (Y, Zr and Nb of plagioclase), Ewart and Griffin (1994) (Y and Zr of magnetite), McKenzie and O'Nions (1991) (Ti of clinopyroxene and plagioclase), and Shimizu and Kushiro (1975) (Nb, Ti of magnetite). Partition coefficients for gabbronorites follow those of Fujimaki et al. (1984, REEs) and Rollison (1995, all other coefficients).

positional variations in these rocks (Fig. 7) are not incompatible with this interpretation. The Xigou gabbro rocks have extremely low compatible element concentrations (e.g., Ni 34–110 ppm, Cr 49–276 ppm); this indicates low compatible contents in the parent magma. Plagioclase in these rocks has an extremely low anorthite content (<10 mol%), incompatible with those crystallized from a gabbroic liquid but similar to those accumulated from a felsic magma. A mode calculation was attempted (Fig. 9), and this shows that a cumulate composed of 5 mol% magnetite, 35 mol% clinopyroxene, and 60 mol% plagioclase in equilibrium with the Liangcheng granitoids could match the trace element variations in the Xigou gabbro. This modeled mode is similar to the normative modes calculated for the Xigou gabbro (Table 3). We suggest that the Xigou gabbro is an early mafic cumulate of the parental magma of the Liangcheng granitoids.

7.2. The Xuwujia gabbronorites: origin, differentiation and assimilation

7.2.1. Fractional crystallization

Both the high-Mg and low-Mg rocks of the Xuwujia gabbronorites show well correlated trends in most variation plots (Fig. 7). For example, in a CaO versus MgO plot (Fig. 7), CaO correlates negatively with MgO for samples with MgO-concentrations >6.0 wt.% (high-Mg group), but positively for those <6.0 wt.% (low-Mg group). The negative correlation could be due to differentiation of olivine and low-CaO pyroxene (e.g., hypersthene), whereas positive correlations could be caused by the fractionation of high-CaO pyroxene (clinopyroxene) and plagioclase. This is consistent with the fractional crystallization trends shown in the variation diagrams (Fig. 10), which indicate that olivine is also a potential crystallizing phase for the low-Mg group.

A simplified two-stage differentiation model, including fractionation of olivine + hypersthene in the high-Mg group and olivine + plagioclase + clinopyroxene in the low-Mg group, is suggested. Fraction (F, vol.%) of magma and proportion (p, mol%) of each mineral is calculated. Three samples are selected as the end members: 07XBY02 as the least evolved, 06LC13 as the most evolved, and 99XBY6-4 as transitional (i.e. the most evolved in the high-Mg group but the primitive component of the low-Mg group; all the concentrations in Table 3 are recalculated to 100 wt.% totals for the major elements. The formulas of the mafic phases are assumed using Mg–Fe equilibrium between minerals and primitive melt (whole-rock). Partition coefficients ($K_{d\,Fe\text{–}Mg}$) of 0.33 (olivine) and 0.36 (pyroxene) are used after Kinzler (1997). Accordingly, the formulas of olivine and hypersthene in the first stage are $(Mg_{0.9}Fe_{0.1})_2SiO_4$ and $(Mg_{0.85}Fe_{0.15})_2Si_2O_6$, whereas olivine and clinopyroxene in the second stage (low-Mg) are $(Mg_{0.7}Fe_{0.3})_2SiO_4$) and $Ca(Mg_{0.7}Fe_{0.3})Si_2O_6$, respectively. For plagioclase, we take $Ca_{0.75}Na_{0.5}Al_2Si_2O_8$, similar to the analyzed composition of representative plagioclase in sample 99XBY6-4.

In the first stage (high-Mg), as chemical variations of CaO and MgO show the best correlations in Fig. 7, balances of them are used to establish the following two equations: (CaO or MgO content in melt, wt.%)$_{primitive} = (1 - F_1) \times$ (CaO or MgO content in melt, wt.%)$_{evolved} + F_1 \times [p_{ol1} \times$ (CaO or MgO in hypersthene, wt.%)$_{fractionated} + (1 - p_{ol1}) \times$ (CaO or MgO in hypersthene, wt.%)$_{fractionated}$]. Here p_{ol1} and $(1 - p_{ol1})$ refer to proportions of olivine and hypersthene, respectively. As assumed above, samples 07XBY02 and 99XBY6-4 represent the primitive and evolved compositions of the magma, respectively. Solving the two equations yields: $F_1 = 0.45$; $p_{ol1} = 0.62$; $(1 - p_{ol1}) = 0.38$. This means that fractional crystallization of 45 vol.% of the magma with 62 mol% olivine and 38 mol% hypersthene, can explain the CaO and MgO variations in the high-Mg group.

In the second stage (low-Mg), as chemical variations of CaO, SiO_2 and MgO show the best correlations in Fig. 7, balances of them are used to establish the following equations: (SiO_2, CaO, or MgO content in melt, wt.%)$_{primitive} = (1 - F_2) \times$ (SiO_2, CaO, or MgO in melt, wt.%)$_{evolved} + F_2 \times [p_{ol2} \times$ (SiO_2, CaO, or MgO in olivine, wt.%) $+ p_{py2} \times$ (SiO_2, CaO, or MgO in clinopyroxene, wt.%) $+ (1 - p_{ol2} - p_{py2}) \times$ (SiO_2, CaO, or MgO content in plagioclase, wt.%)]. Here F_2 refers to the fraction of the separated magma during this stage. And p_{ol2}, p_{py2} and $(1 - p_{ol2} - p_{py2})$ are proportion of olivine, clinopyroxene and plagioclase in the separated assemblage. Primitive and evolved compositions are assumed as those of 99XBY6-4 and 06LC13, respectively. The equations give: $F_2 = 0.71$; $p_{ol2} = 0.17$; $p_{py2} = 0.22$; $(1 - p_{ol2} - p_{py2}) = 0.61$. This means that 71 vol.% of magma separation through fractional crystallization with 17 mol% olivine, 22 mol% clinopyroxene and 61 mol% plagioclase can explain the CaO, MgO and SiO_2 variations in the low-Mg group.

Fig. 9 shows the predicted trace element variations in the Xuwujia gabbronorites using the above modeling results. Curve 4 tracks the predicted compositions of liquid after differentiation of the first stage. It fits well with the compositional variation of the high-Mg group. Curve 5 is the prediction of the second stage of fractional crystallization. It predicts well the concentration of some trace elements, but fails for some others (e.g., the heavy REEs).

7.2.2. Assimilation and contamination

Although fractional crystallization can explain some of the trace element variations (e.g., Fig. 9), it fails to explain some irregular variations in concentrations of TiO_2, Fe_2O_3t, P_2O_5 and Nb contents at a constant MgO content (Fig. 7), variations of Nb, Ti, Zr and heavy REE concentrations in spidergrams (Fig. 8b), and variations of εNd_t values (Fig. 11). These characteristics cannot easily be interpreted by fractionation alone, but could be the result of assimilation and/or contamination by crust. The khondalite is suggested as the most important contaminant, as it directly hosts these igneous rocks. Fig. 11 shows the variations of εNd_t ($t = 1.93$ Ga) values versus SiO_2 and some incompatible elemental ratios, as well as two-member mixing modeling between a potential gabbronorite reservoir represented by the most primitive gabbronorite sample ($\varepsilon Nd_t = 2.4$, $SiO_2 = 47.2$ wt.%, Yb = 1.76 ppm, La = 3.44 ppm, Nb = 1.51 ppm and Zr = 24.6 ppm) and crustal contaminant represented by the khondalite ($\varepsilon Nd_t = -4.6$, $SiO_2 = 75.3$ wt.%, Yb = 0.09 ppm, La = 12.2 ppm, Nb = 0.12 ppm and Zr = 15.2 ppm). Variations in ratios between different incompatible elements can rule out the effects of fractional crystallization. These diagrams suggest that mixing of up to 70 vol.% of a khondalite with the gabbronorite magma could explain most observed variations. Fig. 11b also shows that the relatively heavy REE depletion (represented by lower Yb/La ratios) in the low-Mg rocks of the Xuwujia gabbronorites could be interpreted by assimilation of crust. Curve 6 in Fig. 9 is a composition mixed by 30 vol.% khondalite represented by sample 02SX008 and 70 vol.% of differentiates represented by curve 5. The diagrams also indicate that there is a possible second contaminant besides the khondalite. We suggested that the Paleoproterozoic basement and/or protoliths of the khondalite (metasediments), which is poorly known so far (e.g., ca. 2.0 Ga granites in the very northwest part of the study area, Guo et al., 2001), or Archean TTG gneisses from either south or north of the study area (Zhao et al., 2008; Liu et al., 2009a), could be potential candidates.

7.2.3. Primary magma and melting conditions in the source region

The high-Mg group of the Xuwujia gabbronorites has Mg numbers of ~70, Cr mostly >1000 ppm (up to 3479 ppm), and Ni mostly >300 ppm (up to 1325 ppm). This is similar to experimental results from lherzolite melts. It could be argued that these samples reflect

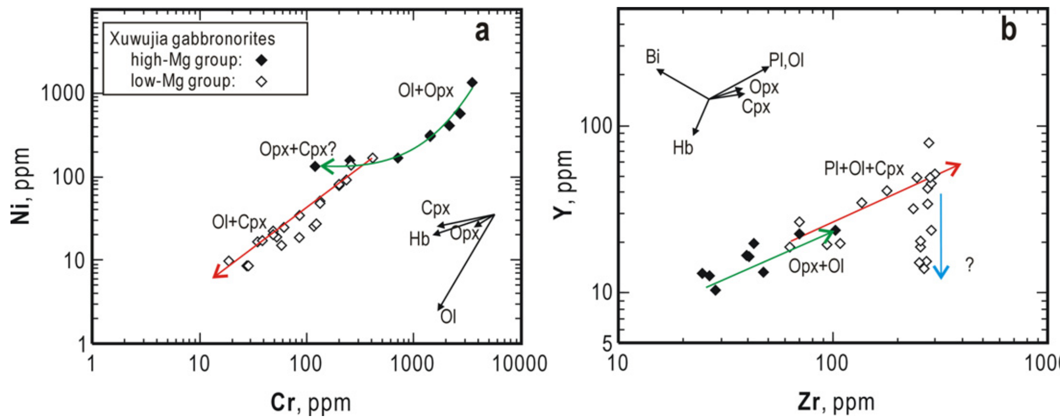

Fig. 10. Elemental variation diagrams showing fractional crystallization trends: (a) Ni versus Cr; (b) Y versus Zr; (c) Nb versus Zr. Opx: orthopyroxene; Cpx: clinopyroxene; Hb: hornblende; Ol: olivine; Bi: biotite; and Pl: plagioclase.

accumulation of olivine and/or orthopyroxene as some are not from chilled margins. But accumulation of these minerals will cause slightly fractionated light and heavy REE patterns, which is not shown in this group (Fig. 8). Some may still argue that there could be felsic mineral-dominated fractionation (mainly feldspar) during the earliest stages, which increased the MgO concentrations in the liquid, as there are negative Eu-anomalies (Fig. 8a). But there are several possibilities for the negative Eu-anomalies, such as mixing of melts or metasomatism of elements from wall rocks, magmatic differentiation (e.g., fractionation of feldspar, Alderton et al., 1980; Hanson, 1980), alteration and fluid-rock interaction (e.g., White and Martin, 1980; Dawood et al., 2004), or high-temperature metamorphism (reduction of Eu^{3+} to Eu^{2+} and fractionation from other REEs with the increase of temperature, e.g., Bau, 1991). As these samples have extremely high MgO but low SiO_2 content, the negative anomalies in the gabbronorites are unlikely to have originated from crustal contamination. In addition, the potential contaminant, khondalite, typically has positive Eu-anomalies (Wan et al., 2000; e.g., sample 02SX008). Thus, either Eu fractionation under high-temperature metamorphism, or fractionation of feldspar is the likely cause of the negative Eu-anomalies for the samples in this group. Based on calculation, about 5 vol.% fractionation of pla-

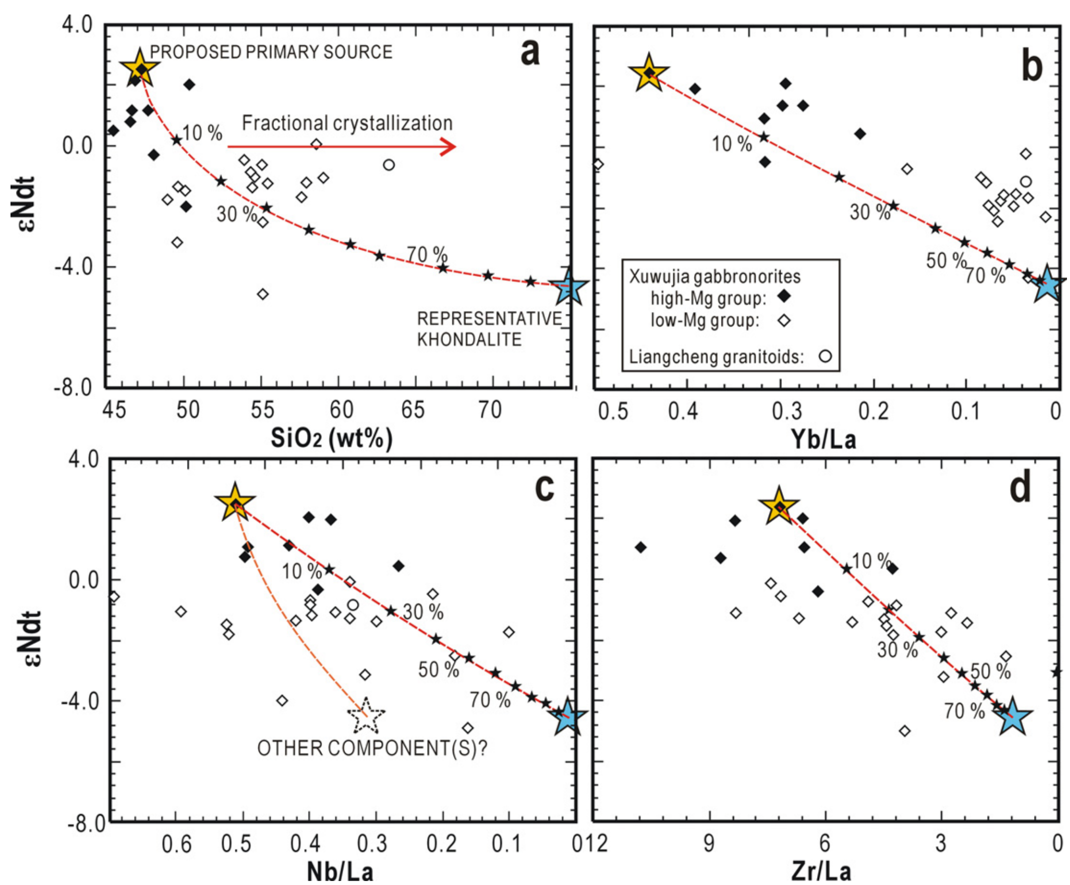

Fig. 11. εNd_t versus SiO_2 (a), Yb/La (b), Nb/La (c), and Zr/La (d) diagrams. Magma mixing curves between the proposed primary compositions of the Xuwujia gabbronorites and the khondalite are calculated. Sample 99XBY-3 is selected as the composition of primitive gabbronoritic melt, whereas samples 02SX008 (trace elements) and HT2-9 (isotopes) are representatives of khondalite melt. Lines with stars show different degrees of mixing between these two end members.

gioclase alone from a liquid without Eu-anomalies could cause the corresponding Eu-anomalies in Fig. 8a (partition coefficients after Fujimaki et al., 1984). This small amount of fractionation will have no substantial influences on major elements, especially MgO concentrations. We suggest the least evolved gabbronorite samples with MgO contents between 18 and 23 wt.% (high-Mg group) could be close to the primary composition of the Xuwujia gabbronorite magmas.

Thus the MgO concentration of these most primitive samples is used as estimations of MgO concentration of the primary liquid of the Xuwujia gabbronorites, and to constrain the melting conditions in the source region. The melting temperature is calculated at 1500–1600 °C using the equation $T\,(^{\circ}\mathrm{C}) = 2000 \times \mathrm{MgO}/(\mathrm{MgO} + \mathrm{SiO_2})\ (\mathrm{wt.\%}) + 969$ (Albarède, 1992), similar to model of Putirka (2005); the melting pressure for the primary sample is ∼3.0 GPa using the equation $\ln P\,(\mathrm{kbar}) = 0.00252 \times T\,(^{\circ}\mathrm{C}) - 0.12 \times \mathrm{SiO_2}\ (\mathrm{wt.\%}) + 5.027$ (Albarède, 1992); the mantle potential temperature is about 1550 °C ($T_P\,(^{\circ}\mathrm{C}) = 1463 + 12.74 \times \mathrm{MgO} - 2924/\mathrm{MgO}$, after Herzberg and O'Hara, 2002; even higher based on other models); and the primary eruption temperature would be about 1400 °C ($T\,(^{\circ}\mathrm{C}) = 935 + 33 \times \mathrm{MgO} - 0.37\mathrm{MgO}^2$, after Beattie, 1993a) (Fig. 12). This potential temperature is higher than the Paleoproterozoic ambient mantle (at ∼1500 °C estimated from a secular Earth cooling model of 50–100 °C/Ga, after Pollack, 1997; even lower after Komiya, 2004). The high eruption temperature could be responsible to the ultra-high-temperature metamorphism in the metapelite along these Xuwujia intrusions.

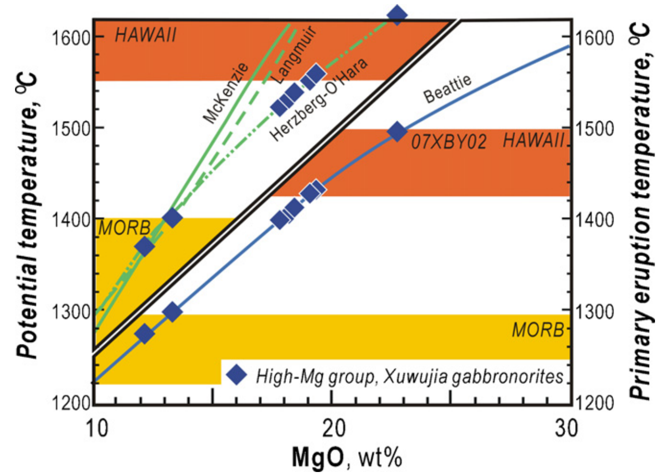

Fig. 12. Primary eruption and mantle potential temperatures as a function of the MgO contents of primary magmas (after Herzberg et al., 2007). Potential temperature models are from Herzberg, McKenzie, Langmuir, and others (cited from Herzberg et al., 2007) and calculated here as T_P, °C = 1463 + 12.74 × MgO − 2924/MgO (Herzberg and O'Hara, 2002). Primary eruption temperatures are of Beattie (1993a) (T, °C = 935 + 33 × MgO − 0.37MgO^2).

7.3. The Xuwujia gabbronorites and Liangcheng granitoids: products of the same thermal event?

Postulating the geodynamic environment of the Xuwujia gabbronorites is beyond the scope of this paper, although melting from a source region with anomalously high potential temperatures is considered to be characteristic of mantle plume regions (e.g., Campbell and Griffiths, 1992), or to be typical of melting of relatively shallow mantle at less extreme but still high temperatures caused by water fluxing in subduction zones (Parman et al., 1997), perhaps following ridge subduction (e.g., Osozawa, 1992; Kinoshita, 1995; Yang et al., 1996). We favour a ridge subduction over a plume model in that (1) the magmas show a belt-like distribution with small scale (∼250 km, see Fig. 1b), and (2) the rocks show arc-affinities (e.g., Nb- and Zr-depletion; Fig. 8b).

However, the observed high-temperature magmatism must be compatible with a magma mingling and mixing model to explain the related occurrences of the Liangcheng granitoids and Xuwujia gabbronorites (Fig. 13). This model is similar to case studies by Cole et al. (2001), Kuşcu and Floyd (2001) and Arvin et al. (2004), and numerical modeling by Annen et al. (2008). Firstly, the high-temperature gabbronoritic magma (primary magma of Xuwujia gabbronorites) originated from the mantle and ascended to underplate khondalite (the lower crust) at ca. 1.95 Ga. This high-temperature magmatism subsequently triggered extensive melting of the crust to produce granitoid melts (parental magma of the Liangcheng granitoids). The gabbronoritic liquid intruded into the crust as dykes, sills and plutons, and partly injected into the grani-

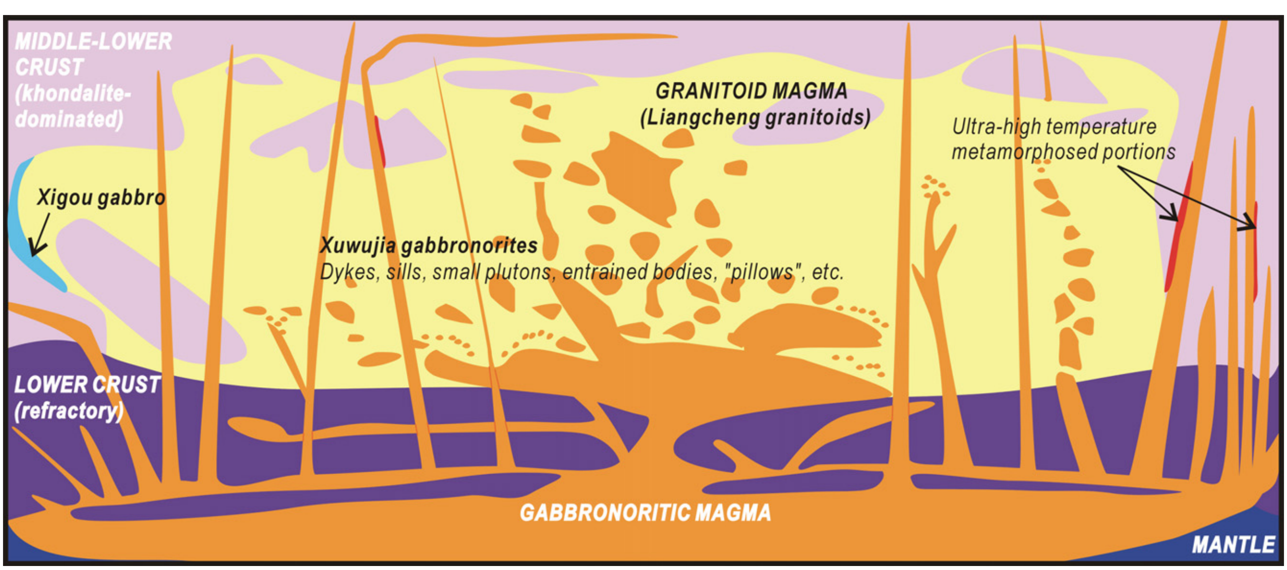

Fig. 13. Petrogenetic model for the Xuwujia gabbronorites and Liangcheng granitoids. The gabbronorite liquid could have ascended from a deeply rooted mantle region with high potential temperature intruded into the lower crust, whereas the granitoids melt was generated from the crust (represented by the khondalite) by the heat supplied from the underplating gabbronorite magma. The gabbronorite liquid intruded into the khondalite and was also injected into the granitoid magma, causing mingling and partial mixing. The gabbronoritic magmatism could be occurred at ca. 1.95–1.93 Ga, whereas the youngest granitoids solidified at ca. 1.90 Ga or even later.

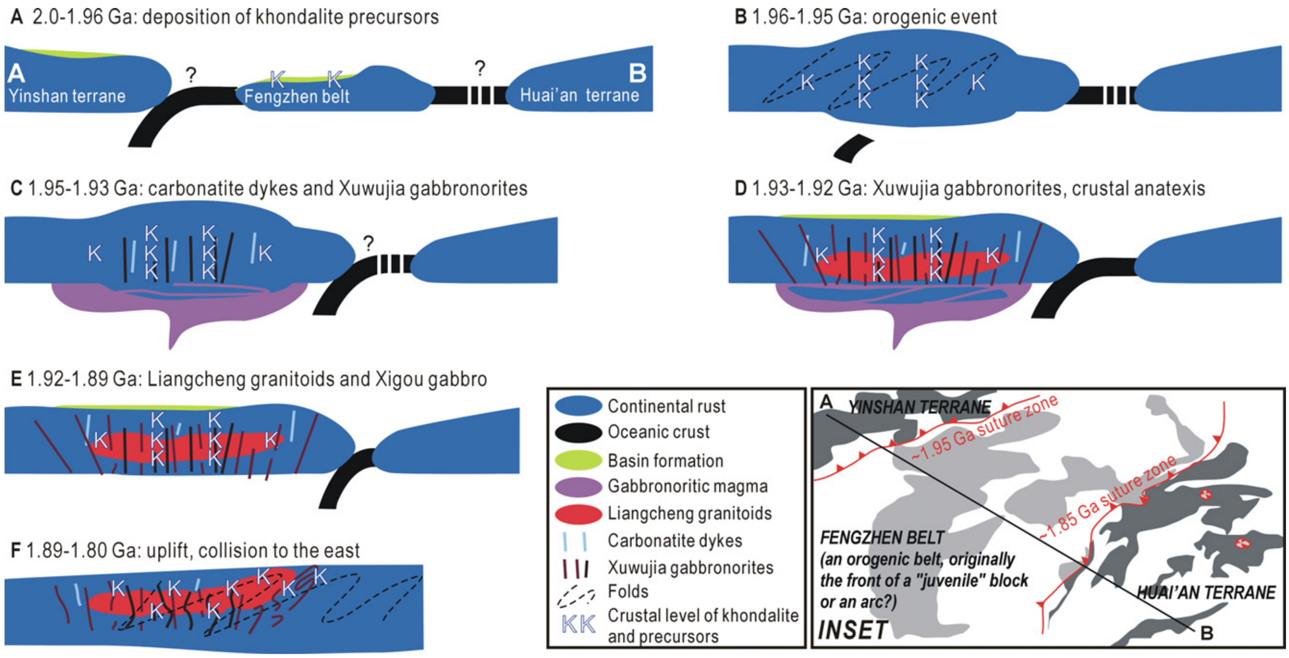

Fig. 14. Cartoons showing the late Paleoproterozoic (2.0–1.8 Ga) evolution of the study area. Inset: tectonic subdivision of the study area (Fig. 1b) and the position of section lines A and B.

toid region, causing mingling and partial mixing: the gabbronoritic intrusives would have cooled and solidified quickly as they were emplaced in cooler granitoid magma and crust, with partial melt mixing between the granitoid and gabbronoritic melts. Then the granitoid magmas started crystallization. The Xigou gabbro represents early crystal accumulation located along the margin of one of the granitoid plutons. The latest granitoids solidified much later (at ca. 1.90 Ga or even later) due to slow heat diffusion in the deep crust. This model can explain the occurrences of the Xuwujia gabbronorites and Liangcheng granitoids: some gabbronorites are preserved as entrained bodies and "pillows" in the granitoids; while there are also "blobs" of granitoids in the gabbronorites (Fig. 2). The high-Mg rocks of the Xuwujia gabbronorites are mostly seen in the khondalite, but not in the granitoids. This observation can be understood if high-Mg melts also intruded into the granitoid melts but mixed with them and were preserved chemically as low-Mg rocks.

7.4. Possible geological scenario of the study area

Two high-grade metamorphic events, one at ca. 1.96–1.95 Ga (Wan et al., 2008; Yin et al., 2008) and another at ca. 1.93–1.92 Ga (Santosh et al., 2006, 2007a; Guo et al., 2006; Liu et al., 2009b), are recorded in the khondalite. The ca. 1.93–1.92 Ga high-temperature metamorphism is possibly related to the gabbronoritic magmatism (with high eruption temperature, see Section 7.3), as these events have very similar ages. This agrees with the observation that all localities of high-temperature metamorphism in the metasedimentary rocks are accompanied by gabbronoritic dykes. Subsequent metamorphism recorded in the Xuwujia gabbronorites could have happened during the late orogenic processes in the central NCC (e.g., Zhao et al., 2005) or during a subsequent uplift of the study area. The Xigou gabbro records a 1.86 Ga metamorphism at an upper crustal level, distinct from the ca. 1.93–1.92 Ga regional metamorphism in the lower crust (e.g., Santosh et al., 2006). This suggests an exhumation from lower (~1.93–1.92 Ga) to upper (~1.86 Ga) crustal levels during the 1.92–1.86 Ga interval. The uplift event possibly resulted in the final stability of the Fengzhen belt and the western part of the NCC.

Thus, a possible geological scenario for the study area includes (Fig. 14): (1) deposition of the sedimentary precursors to the khondalite between 2.0 and 1.96 Ga (Wan et al., 2006), possibly in the shelf of a "juvenile" block or a back-arc basin (Fig. 14A); (2) burial of the sediments to lower crustal levels at ca. 1.96–1.95 Ga, possibly due to continent–continent (arc?) collision (e.g., Wan et al., 2006; Yin et al., 2008) (Fig. 14B); (3) intrusion of crustal carbonatite dykes (Wan et al., 2008), possibly due to the ponding of mantle-derived gabbronoritic magmas at the crust–mantle boundary, and intrusion of some gabbronoritic dykes into the crust at ca. 1.96–1.92 Ga (~1.93 Ga; Fig. 14C); (4) crustal anatexis, genesis of granitoid melts, and high-temperature metamorphism in the khondalite (at ultra-high-temperature proximal to some gabbronoritic dykes) (e.g., Guo et al., submitted for publication), and possible delamination of parts of the refractory lower crust (Fig. 14D); (5) emplacement of granitoids between 1.93 and 1.89 Ga (e.g., Zhong et al., 2007) (Fig. 14E); and (6) uplift (exhumation) and collision with the Huai'an terrane to the east during 1.89–1.80 Ga (Fig. 14F).

8. Concluding remarks

Intrusion of the Xuwujia gabbronorites in the northern margin of the NCC likely occurred at ca. 1.96–1.92 Ga (~1.93 Ga), followed by the Liangcheng granitoids at ca. 1.93–1.89 Ga. These gabbronorites experienced assimilation of crust and fractional crystallization of olivine and hypersthene, followed by olivine, clinopyroxene, and plagioclase. They have a mantle origin, from a source region with a high potential temperatures (~1550 °C), and could result in extremely high primary intrusive temperature (~1400 °C). The elevated mantle temperatures could have been caused by a mantle plume, or more likely an asthenospheric upwelling in response to ridge-subduction. Underplating and injection of the high-temperature melts resulted in extensive crustal anatexis, producing large volumes of calc-alkaline granitoids (Liangcheng granitoids), and local ultra-high-temperature metamorphism. This extensive crust–mantle interaction could have happened after ca. 1.95 Ga continent–continent (arc?) juxtaposition in the northern margin of the NCC, and was followed at 1.90–1.80 Ga by regional uplift with the exhumation of the study area from lower to upper crustal levels and collision to the east.

Acknowledgements

This work was supported by grants nos. 40730315, 90714003, 40721062, and 40602024 from the National Foundation. Drs. G.-C. Zhao, Y.-S. Wan, B. Windley, C.-Y. Dong, Q.-L. Li, J.-H. Yang, F. Liu, B. Hu, and many others are thanked for their interesting discussions and for their help in either the field or in the labs. Guest editor M.A. Hamilton, and R. Ernst and an anonymous reviewer are thanked for a constructive critique.

References

Albarède, F., 1992. How deep do common basaltic magmas form and differentiate? Journal of Geophysical Research 97, 10997–11009.

Alderton, D.H.M., Pearce, J.A., Potts, P.J., 1980. Rare earth elements mobility during granite alteration: evidence from southwest England. Earth and Planetary Science Letters 49, 149–165.

Anderson, A.T., 1987. Parental basalts in subduction zones: implications for continental evolution. Journal of Geophysical Research 87, 7047–7060.

Annen, C., Blundy, J.D., Sparks, S.J., 2008. The sources of granitic melt in Deep Hot Zones. Transactions of the Royal Society of Edinburgh, Earth Sciences 97, 297–309.

Arvin, M., Dargahi, S., Babaei, A.A., 2004. Mafic micro-granular enclave swarms in the Chenar granitoid stock, NW of Kerman, Iran: evidence for magma mingling. Journal of Asian Earth Sciences 24, 105–113.

Bau, M., 1991. Rare earth element mobility during hydrothermal and metamorphic fluid-rock interaction and the significance of the oxidation state of europium. Chemical Geology 93, 219–230.

Beattie, P., 1993a. Olivine-melt and orthopyroxene-melt equilibria. Contribution to Mineralogy and Petrology 115, 103–111.

Beattie, P., 1993b. The effect of partial melting of spinel peridotite on uranium series disequilibria: constraints from partitioning studies. Earth and Planetary Science Letters 177, 379–391.

Black, L.P., Kamo, S.L., Allen, C.M., Aleinikoff, J.N., Davis, D.W., Korsch, R.J., Foudoulis, C., 2003. TEMORA 1: a new zircon standard for Phanerozoic U–Pb geochronology. Chemical Geology 200, 155–170.

Blichert-Toft, J., Albarède, F., 1997. The Lu–Hf geochemistry of chondrites and the evolution of the mantle–crust system. Earth and Planetary Science Letters 148, 243–258.

Campbell, I.H., Griffiths, R.W., 1992. The changing nature of mantle hotspots through time: implications for the geochemical evolution of the mantle. Journal of Geology 92, 497–523.

Chesworth, W., Dejou, J., Larroque, P., 1981. The weathering of basalt and relative mobilities of the major elements at Belbex, France. Geochimica et Cosmochimica Acta 45 (7), 1235–1243.

Chu, N.C., Taylor, R.N., Chavagnac, V., Nesbitt, R.W., Boella, R.M., Milton, J.A., German, C.R., Bayon, G., Burton, K., 2002. Hf isotope ratio analysis using multi-collector inductively coupled plasma mass spectrometry: an evaluation of isobaric interference corrections. Journal of Analytical Atomic Spectrumetry 17, 1567–1574.

Cole, J.W., Gamble, J.A., Burt, R.M., Carroll, L.D., Shelley, D., 2001. Mixing and mingling in the evolution of andesite-dacite magmas; evidence from co-magmatic plutonic enclaves, Taupo Volcanic Zone, New Zealand. Lithos 59, 25–46.

Condie, K.C., Boryta, M.D., Liu, J.Z., Qian, X.L., 1992. The origin of khondalites: geochemical evidence from the Archean to Early Proterozoic granulite belt in the North China craton. Precambrian Research 59, 207–223.

Dawood, Y.H., Abd El-Naby, H.H., Sharafeldin, A.A., 2004. Influence of the alteration processes on the origin of uranium and europium anomalies in trachyte, central Eastern Desert, Egypt. Journal of Geochemical Exploration 88, 15–27.

DePaolo, D.J., 1981. Nd isotopes in the Colorado Front Range and crust–mantle evolution in the Proterozoic. Nature 291, 193–196.

Dunn, T., Sen, C., 1994. Mineral/matrix partition-coefficients for ortho-pyroxene, plagioclase, and olivine in basaltic to andesitic systems – a combined analytical and experimental-study. Geochimica et Cosmochimica Acta 58 (2), 717–733.

Ewart, A., Griffin, W.L., 1994. Application of proton-microprobe data to trace-element partitioning in volcanic-rocks. Chemical Geology 117 (1–4), 251–284.

Fujimaki, H., Tatsumoto, M., Aoki, K., 1984. Partition coefficients of Hf, Zr and REE between phenocrysts and groundmasses. Proceedings of the fourteenth lunar and planetary science conference, Part 2. Journal of Geophysical Research 89 (suppl.), B662–B672.

Griffin, W.L., Pearson, N.J., Belousova, E., Jackson, S.E., van Achterbergh, E., O'Reilly, S.Y., Shee, S.R., 2000. The Hf isotope composition of cratonic mantle: LAM-MC-ICPMS analysis of zircon megacrysts in kimberlites. Geochimica et Cosmochimica Acta 64 (1), 133–147.

Guo, J.H., Shi, X., Bian, A.G., Xu, R.H., Zhai, M.G., Li, Y.G., 1999. Pb isotopic composition of feldspar and U–Pb age of zircon from early Proterozoic granite in Sanggan area, North China craton: metamorphism, crustal melting and tectonothermal event. Acta Petrologica Sinica 15, 199–207 (in Chinese with English abstract).

Guo, J.-H., Zhai, M.-G., Xu, R.-H., 2001. Timing of the granulite-facies metamorphism in the Sanggan area, North China craton: zircon U–Pb geochronology. Science in China (Series D) 44 (11), 1010–1018.

Guo, J.-H., Sun, M., Chen, F.-K., Zhai, M.-G., 2005. Sm–Nd and SHRIMP U–Pb zircon geochronology of high-pressure granulites in the Sanggan area, North China craton: timing of Paleoproterozoic continental collision. Journal of Asian Earth Sciences 24 (5), 629–642.

Guo, J.H., Chen, Y., Peng, P., Liu, F., Chen, L., Zhang, L.Q., 2006. Sapphirine-bearing granulite in Daqingshan, Inner Mongolia: 1. 8 Ga UHT metamorphic event. In: Abstract Volume of 2006 Petrology and Earth dynamics in China. Nanjing University, Nanjing, pp. 215–218.

Guo, J.-H., Zhao, G.-C., Chen, Y., Peng, P, Windley, B., Sun, M., submitted for publication. Highly silica-undersaturated sapphirine granulites from the Daqingshan area of the western block, North China craton: Paleoproterozoic UHT metamorphism and tectonic implications. Journal of Petrology.

Hanson, G.N., 1980. Rare earth elements in petrogenetic studies of igneous systems. Annual Reviews of Earth and Planet Sciences 8, 371–406.

Herzberg, C., O'Hara, M.J., 2002. Plume-associated ultramafic magmas of Phanerozoic age. Journal of Petrology 43, 1857–1883.

Herzberg, C., Asimow, P.D., Arndt, N., Niu, Y., Lesher, C.M., Fitton, J.G., Cheadle, M.J., Saunders, A.D., 2007. Temperatures in ambient mantle and plumes: constraints from basalts, picrites, and komatiites. Geochemistry Geophysics Geosystems 8, Q02006, doi:10.1029/2006GC001390.

Hoskin, P.W.O., Schaltegger, U., 2003. The composition of zircon and igneous and metamorphic petrogenesis. In: Hanchar, J.M., Hoskin, P.W.O. (Eds.), Zircon, Mineralogical Society of America, Reviews in Mineralogy and Geochemistry, vol. 53, pp. 27–62.

Iizuka, T., Hirata, T., 2005. Improvements of precision and accuracy *in situ* Hf isotope microanalysis of zircon using the laser ablation-MC-ICPMS technique. Chemical Geology 220, 121–137.

Irvine, T.N., Baragar, W.R.A., 1971. A guide to the chemical classification of the common volcanic rocks. Canadian Journal of Earth Sciences 8, 523–548.

Kinoshita, O., 1995. Migration of Igneous activities related to ridge subduction in Southwest Japan and the East Asian continental margin from the Mesozoic to the Paleogene. Tectonophysics 245, 25–35.

Kinzler, R., 1997. Melting of mantle peridotite at pressures approaching the spinel to garnet transition: application to mid-ocean ridge basalt petrogenesis. Journal of Geophysical Research 102, 853–874.

Komiya, T., 2004. Material circulation model including chemical differentiation within the mantle and secular variation of temperature and composition of the mantle. Physics of the Earth and Planetary Interiors 146, 333–367.

Kröner, A., Wilde, S.A., Li, J.-H., Wang, K.-Y., 2005. Age and evolution of a late Archean to Paleoproterozoic upper to lower crustal section in the Wutaishan/Hengshan/Fuping terrain of north China. Journal of Asian Earth Sciences 24 (5), 577-576.

Kuşcu, G.G., Floyd, P.A., 2001. Mineral compositional and textural evidence for magma mingling in the Saraykent volcanics. Lithos 56, 207–230.

Kusky, T.M., Li, J.-H., 2003. Paleoproterozoic tectonic evolution of the North China Craton. Journal of Asian Earth Sciences 22, 383–397.

Kusky, T.M., Li, J.-H, Tucker, R.T., 2001. The Archean Dongwanzi ophiolite complex, North China craton: 2.505 billion year old oceanic crust and mantle. Science 292, 1142–1145.

Kusky, T., Li, J.-H., Santosh, M., 2007. The Paleoproterozoic North Hebei Orogen: North China craton's collisional suture with the Columbia supercontinent. Gondwana Research 12, 4–28.

Lan Z.-W., 2006. Petrogenesis of garnet-bearing granites in the khondalites of North China craton: mixing mechanism of melt and residue. PhD Thesis of the Institute of Geology and Geophysics, Chinese Academy of Sciences, pp. 1–43.

Larsen, L.M., 1979. Distribution of REE and other trace-elements between phenocrysts and peralkaline undersaturated magmas, exemplified by rocks from the Gardar Igneous Province, South Greenland. Lithos 12 (4), 303–315.

Latypov, R., Chistyakova, S., Alapieti, T., 2007. Revisiting problem of chilled margins associated with marginal reversals in mafic–ultramafic intrusive bodies. Lithos 99, 178–206.

Li, J.-H., Qian, X.-L., Huang, X.-N., Liu, S.-W., 2000. Tectonic framework of North China Block and its cratonization in the Early Precambrian. Acta Petrologica Sinica 16, 1–10 (in Chinese with English abstract).

Li, J.-H., Kusky, T.M., Huang, X.-N., 2002. Neoarchean podiform chromitites and mantle tectonites in ophiolitic mélange, North China craton: a record of early Oceanic mantle oceanic mantle processes. GSA Today 12, 4–11.

Li, X.-H., Liu, Y., Li, Q.-L., Guo, C.-H., Chamberlain, K.R., 2009. Precise determination of Phanerozoic zircon Pb/Pb age by multicollector SIMS without external standardization. Geochemistry Geophysics Geosystems 10, Q04010, doi:10.1029/2009GC002400.

Liu, S.-W., Pan, Y.-M., Xie, Q.-L., Zhang, J., Li, Q.-G., Yang, B., 2005. Geochemistry of the Paleoproterozoic Nanying granitic gneisses in the Fuping Complex: implications for the tectonic evolution of the Central Zone, North China craton. Journal of Asian Earth Sciences 24, 643–658.

Liu, F., Guo, J.-H., Lu, X.-P., Diwu, C.-R., 2009a. Crustal growth at ~2.5 Ga in the North China craton: evidence from whole-rock Nd and zircon Hf isotopes in the Huai'an gneiss terrane. Chinese Science Bulletin 54, 4704–4713.

Liu, S.J., Li, J.-H., Santosh, M., 2009b. First application of the revised Ti-in-zircon geothermometer to Paleoproterozoic ultrahigh-temperature granulites of Tuguiwula, Inner Mongolia, North China craton. Contributions to Mineralogy and Petrology, doi:10.1007/s00410-009r-r0425-2.

Lu, L.Z., Xu, X.C., Liu, F.L., 1996. The Precambrian Khondalite Series in North China. Changchun Publishing House, Changchun, pp. 1–99 (in Chinese).

Ludwig, K.R., 2002. SQUID 1.02, A User's Manual, vol. 2. Berkeley Geochronology Center, Special Publication.

Ludwig, K.R., 2003. User's Manual for Isoplot/EX Version 3.00. A Geochronological Toolkit for Microsoft Excel, vol. 4. Berkeley Geochronology Center Special Publication, 71 pp.

Luhr, J.F., Carmichael, I.S.E., 1980. The Colima volcanic complex, Mexico. I: post-caldera andesites from Volcan Colima. Contributions to Mineralogy and Petrology 71, 343–372.

McKenzie, D., O'Nions, R.K., 1991. Partial melt distributions from inversion of rare Earth element concentrations. Journal of Petrology 32, 1021–1091.

Middelburg, J.J., van der Weijden, C.H., Woittiez, J.R.W., 1988. Chemical processes affecting the mobility of major, minor and trace elements during weathering of granitic rocks. Chemical Geology 68, 253–273.

Osozawa, S., 1992. Double ridge subduction recorded in the Shimanto accretionary complex, Japan, and late reconstruction. Geology 20, 939–942.

Pandarinath, K., Dulski, P., Torres-Alvarado, I.S., Verma, S.P., 2008. Element mobility during the hydrothermal alteration of rhyolitic rocks of the Los Azufres geothermal field, Mexico. Geothermics 37, 53–72.

Parman, S.W., Dann, J.C., Grove, T.L., de Wit, M.J., 1997. Emplacement conditions of komatiite magmas from the 3.49 Ga Komati Formation, Barerton Greenstone belt, South Africa. Earth and Planetary Science Letters 150, 303–323.

Peng, P., Zhai, M.-G., Zhang, H.-F., Guo, J.-H., 2005. Geochronological constraints on the Paleoproterozoic evolution of the North China craton: SHRIMP zircon ages of different types of mafic dikes. International Geology Review 47 (5), 492–508.

Peng, P., Zhai, M.-G., Guo, J.-H., Kusky, T., Zhao, T.-P., 2007. Nature of mantle source contributions and crystal differentiation in the petrogenesis of the 1.78 Ga mafic dykes in the central North China craton. Gondwana Research 12, 29–46.

Peng, P., Zhai, M.-G., Ernst, R., Guo, J.-H., Liu, F., Hu, B., 2008. A 1.78 Ga large igneous province in the North China craton: the Xiong'er Volcanic Province and the North China dyke swarm. Lithos 101 (3–4), 260–280.

Pollack, H.N., 1997. Thermal characteristics of the Archean. In: Wit, M.D., Ashwall, L.D. (Eds.), Greenstone Belts. Oxford Monogr. Geol. Geophys., Oxford, Clarendon, UK, pp. 223–232.

Putirka, K.D., 2005. Mantle potential temperatures at Hawaii, Iceland, and the mid-ocean ridge system, as inferred from olivine phenocrysts: evidence for thermally driven mantle plumes. Geochemistry Geophysics Geosystems 6, Q05L08, doi:10.1029/2005GC000915.

Qian, X.-L., Li, J.-H., 1999. The acknowledgement of Neo-Archean unconformity event in North China craton and its tectonic significance. Science in China (Series D) 29, 1–8 (in Chinese).

Rollinson, H., 1995. Using geochemical data, evaluation, presentation, and interpretation. Longman Scientific and Technical 63, 108.

Rudnick, R.L, Fountain, D., 1995. Nature and composition of the continental crust: a lower crustal perspective. Reviews of Geophysics 33, 267–309.

Santosh, M., Sajeev, K., Li, J.H., 2006. Extreme crustal metamorphism during Columbia supercontinent assembly: evidence from North China craton. Gondwana Research 10, 256–266.

Santosh, M., Tsunogae, T., Li, J.H., Liu, S.J., 2007a. Discovery of sapphirine-bearing Mg–Al granulites in the North China craton: implications for Paleoproterozoic ultrahigh temperature metamorphism. Gondwana Research 11, 263–285.

Santosh, M., Wilde, S.A., Li, J.-H., 2007b. Timing of Paleoproterozoic ultrahigh-temperature metamorphism in the North China craton: evidence from SHRIMP U–Pb zircon geochronology. Precambrian Research 159, 178–196.

Shi, X., 1997. Geochemistry and petrogenesis study on granitoid in the khondalite sequences in the south of the Neimenggu. Master Thesis of the Institute of Geology and Geophysics, Chinese Academy of Sciences, pp. 1–58.

Shimizu, N., Kushiro, I., 1975. Partitioning of rare-earth elements between garnet and liquid at high-pressures-preliminary experiments. Geophysical Research Letters 2 (10), 413–416.

Söderlund, U., Patchett, P.J., Vervoort, J.D., Isachsen, C.E., 2004. The 176Lu decay constant determined by Lu–Hf and U–Pb isotope systematics of Precambrian mafic intrusions. Earth and Planetary Science Letters 219, 311–324.

Sun, S.-S., McDonough, W.F., 1989. Chemical and isotopic systematics of oceanic basalts implications for mantle composition and process. In: Saunders, A.D., Nony, M.J. (Eds.), Magmatism in the Ocean Basins, vol. 42. Geological Society Special Publication, pp. 313–354.

Taylor, S.R., McLennan, S.M., 1995. The geochemical evolution of the continental crust. Reviews of Geophysics 33, 241–265.

Vervoort, J.D., Patchett, P.J., Söderlund, U., Baker, M., 2004. Isotopic composition of Yb and the determination of Lu concentrations and Lu/Hf ratios by isotopic dilution using MC-ICPMS. G3 5, 2004GC000721.

Wan, Y.-S., Geng, Y.-S., Liu, F.-L., Shen, Q.-H., Liu, D.-Y., Song, B., 2000. Age and composition of the khondalite series of the North China craton and its adjacent area. Progress in Precambrian Research 23 (4), 221–237 (in Chinese with English abstract).

Wan, Y.S., Song, B., Liu, D.Y., Wilde, S., Wu, J.-S., Shi, Y.-R., Yin, X.-Y., Zhou, H.-Y., 2006. SHRIMP U–Pb zircon geochronology of Paleoproterozoic metasedimentary rocks in the North China craton: Evidence for a major Late Paleoproterozoic tectonothermal event. Precambrian Research 149, 249–271.

Wan, Y.S., Liu, D.Y., Xu, Z.Y., Dong, C.Y., Wang, Z.J., Zhou, H.Y., Yang, Z.-S., Liu, Z.H., Wu, J.-S., 2008. Paleoproterozoic crustally derived carbonate-rich magmatic rocks from the Daqingshan area, North China craton: geological, petrographical, geochronological and geochemical (Hf, Nd, O and C) evidence. American Journal of Science 308, 351–378.

Wan, Y.-S., Liu, D.-Y., Dong, C.-Y., Xu, Z.-Y., Wang, Z.-J., Wilde, S., Yang, Y.-H., Liu, Z.-H., Zhou, H.-Y., 2009. The Precambrian Khondalite Belt in the Daqingshan Area, North China craton: Evidence for Multiple Metamorphic Events in the PALEO-PROTEROZOIC ERA, vol. 323. Geological Society Special Publications, London, pp. 73–97.

White, M.V.W., Martin, R.F., 1980. The metasomatic changes that accompany uranium mineralization in the nonorogenic rhyolites of the Upper Alillik Group, Labrador. The Canadian Mineralogist 18, 459–479.

Wilde, S.A., Zhao, G.-C., Sun, M., 2002. Development of the North China craton during the Late Archean and its final amalgamation at 1.8 Ga: some speculation on its position within a global Paleoproterozoic Supercontinent. Gondwana Research 5, 85–94.

Williams, I.S., 1998. U–Th–Pb geochronology by ion microprobe. In: McKibben, M.A., Shanks, W.C., Ridley, W.I. (Eds.), Applications of Microanalytical Techniques to Understanding Mineralizing Processes, vol. 7. Rev. Econ. Geol., pp. 1–35.

Williams, I.S., Hergt, J.M., 2000. U–Pb dating of Tasmanian dolerites: a cautionary tale of SHRIMP analysis of high-U zircon. In: Woodhead, J.D., Hergt, J.M., Noble, W.P. (Eds.), Beyond 2000: New Frontiers in Isotope Geoscience, Lorne; Abstracts and Proceedings, pp. 185–188.

Wood, D.A., Joron, J.L., Treuil, M., 1979. A re-appraisal of the use of trace elements to classify and discriminate between magma series erupted in different tectonic settings. Earth and Planetary Science Letters 50, 326–336.

Wu, C.H., Zhong, C.T., Liu, F.L., 1997. Discussion on the age of khondalite in Jin-Meng high-grade terrain. Acta Petrologica Sinica 13, 289–302 (in Chinese with English abstract).

Wu, F.Y., Yang, Y.H., Xie, L.W., Yang, J.H., Xu, P., 2006. Hf isotopic compositions of the standard zircons and baddeleyites used in U–Pb geochronology. Chemical Geology 234, 105–126.

Xia, X.-P., Sun, M., Zhao, G.-C., Luo, Y., 2006. LA-ICP-MS U–Pb geochronology of detrital zircons from the Jining Complex, North China craton and its tectonic significance. Precambrian Research 144, 199–212.

Xia, X.-P., Sun, M., Zhao, G.-C., Wu, F.-Y., Xu, P., Zhang, J., He, Y.-H., 2008. Paleoproterozoic crustal growth in the western block of the North China craton: evidence from detrital zircon Hf and whole-rock Sr–Nd isotopic compositions of the khondalites from the Jining complex. American Journal of Sciences 308, 304–327.

Yang, T.F., Lee, T., Chen, C.H., Cheng, S.N., Knittel, U., Punongbayan, R.S., Rasdas, A.R., 1996. A double island arc between Taiwan and Luzon: consequence of ridge subduction. Tectonophysics 258, 85–101.

Yin, C.-Q., Zhao, G.-C., Wei, C.-J., Sun, M., Leung, W.-H., 2008. Metamorphism evolution of the Khondalite Belt in the Western Block, North China craton. In: Abstract for the 13th Gondwana Conference, Dali, China, September, 14–21.

Zhai, M.-G., Liu, W.J., 2003. Paleoproterozoic tectonic history of the North China craton: a review. Precambrian Research 122, 183–199.

Zhai, M.-G., Peng, P., 2007. Paleoproterozoic events in the North China craton. Acta Petrologica Sinica 23 (11), 2665–2682.

Zhai, M.G., Guo, J.H., Yan, Y.H., Li, Y.-G., 1992. The discovery of high-pressure basic granulite in the Archean north China craton and preliminary study. Sciences in China (Series B) 12, 1325-1300.

Zhai, M.-G., Guo, J.-H., Li, Y.-G., Liu, W.-J., Peng, P., Shi, X., 2003. Two linear granite belts in the central-western North China craton and their implication for late Neoarchean–Paleoproterozoic continental evolution. Precambrian Research 127, 267–283.

Zhai, M.-G., Guo, J.-H., Liu, W.-J., 2005. Neoarchean to Paleoproterozoic continental evolution and tectonic history of the North China craton: a review. Journal of Asia Earth Sciences 24 (5), 547–562.

Zhao, G.-C., Wilde, S.A., Cawood, P.A., Lu, L.-Z., 1998. Thermal evolution of the Archean basement rocks from the eastern part of the North China craton and its bearing on tectonic setting. International Geological Review 40, 706–721.

Zhao, G.-C., Wilde, S.A., Cawood, P.A., Lu, L.-Z., 1999. Tectonothermal history of the basement rocks in the western zone of the North China craton and its tectonic implications. Tectonophysics 310, 37–53.

Zhao, G.-C., Wilde, S.A., Cawood, P.A., Sun, M., 2001. Archean blocks and their boundaries in the North China craton: lithological, geochemical, structural and *P–T* path constraints and tectonic evolution. Precambrian Research 107, 45–73.

Zhao, G.-C., Sun, M., Wilde, S.A., Li, S.-Z., 2005. Late Archean to Paleoproterozoic evolution of the North China craton: key issues revisited. Precambrian Research 136, 177–202.

Zhao, G.-C., Wilde, S.A., Sun, M., Guo, J.-H., Kroner, A., Li, S.-Z., Li, X.-P., Zhang, J., 2008. SHRIMP U–Pb Zircon geochronology of the Huai'an Complex: constraints on Late Archean to Paleoproterozoic magmatic and metamorphic events in the Trans-North China Orogen. American Journal of Science 308, 270–303.

Zhong, C.-T., Deng, J.-F., Wu, Y.-P., Mao, D.-B., Xi, Z., Chen, B., 2006. Geochemical characteristics and tectonic significations of Paleoproterozoic strongly peraluminous granitoids in the central segment of the northern margin of the North China craton. Geological Bulletin of China 25 (3), 389–397.

Zhong, C.-T., Deng, J.-F., Wan, Y.-S., Mao, D.-B., Li, H.-M., 2007. Magma recording of Paleoproterozoic orogeny in central segment of northern margin of North China craton: geochemical characteristics and zircon SHRIMP dating of S-type granitoids. Geochimica 36 (6), 633–637.